

University of Nebraska - Lincoln

DigitalCommons@University of Nebraska - Lincoln

Papers in Natural Resources

Natural Resources, School of

5-27-2023

Can upscaling ground nadir SIF to eddy covariance footprint improve the relationship between SIF and GPP in croplands?

Genghong Wu

University of Illinois at Urbana-Champaign

Kaiyu Guan

University of Illinois at Urbana-Champaign, DOE Center for Advanced Bioenergy and Bioproducts Innovation

Chongya Jiang

University of Illinois at Urbana-Champaign, DOE Center for Advanced Bioenergy and Bioproducts Innovation

Hyungsuk Kimm

University of Illinois at Urbana-Champaign, Seoul National University

Guofang Miao

University of Illinois at Urbana-Champaign

See this page for additional authors: <https://digitalcommons.unl.edu/natrespapers>



Part of the [Natural Resources and Conservation Commons](#), [Natural Resources Management and Policy Commons](#), and the [Other Environmental Sciences Commons](#)

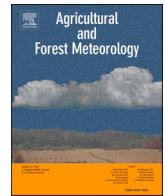
Wu, Genghong; Guan, Kaiyu; Jiang, Chongya; Kimm, Hyungsuk; Miao, Guofang; Yang, Xi; Bernacchi, Carl J.; Sun, Xiangmin; Suyker, Andrew E.; and Moore, Caitlin E., "Can upscaling ground nadir SIF to eddy covariance footprint improve the relationship between SIF and GPP in croplands?" (2023). *Papers in Natural Resources*. 1684.

<https://digitalcommons.unl.edu/natrespapers/1684>

This Article is brought to you for free and open access by the Natural Resources, School of at DigitalCommons@University of Nebraska - Lincoln. It has been accepted for inclusion in Papers in Natural Resources by an authorized administrator of DigitalCommons@University of Nebraska - Lincoln.

Authors

Genghong Wu, Kaiyu Guan, Chongya Jiang, Hyungsuk Kimm, Guofang Miao, Xi Yang, Carl J. Bernacchi, Xiangmin Sun, Andrew E. Suyker, and Caitlin E. Moore



Can upscaling ground nadir SIF to eddy covariance footprint improve the relationship between SIF and GPP in croplands?

Genghong Wu^{a,b,d,*}, Kaiyu Guan^{a,b,c,d,*}, Chongya Jiang^{a,b,d}, Hyungsuk Kimm^{b,e,f},
Guofang Miao^b, Xi Yang^g, Carl J. Bernacchi^{a,h,i}, Xiangmin Sun^a, Andrew E. Suyker^j,
Caitlin E. Moore^{a,h,k}

^a Agroecosystem Sustainability Center, Institute for Sustainability, Energy, and Environment, University of Illinois at Urbana-Champaign, Urbana, IL, United States

^b Department of Natural Resources and Environmental Sciences, College of Agricultural, Consumer and Environmental Sciences, University of Illinois at Urbana-Champaign, Urbana, IL, United States

^c National Center of Supercomputing Applications, University of Illinois at Urbana-Champaign, Urbana, IL, United States

^d DOE Center for Advanced Bioenergy and Bioproducts Innovation, Urbana, IL, United States

^e Research Institute of Agriculture and Life Sciences, Seoul National University, Seoul, South Korea

^f Department of Agriculture, Forestry and Bioresources, College of Agriculture and Life Sciences, Seoul National University, Seoul, South Korea

^g Department of Environmental Sciences, University of Virginia, Charlottesville, Virginia, United States

^h Department of Plant Biology, University of Illinois at Urbana-Champaign, Urbana, IL, United States

ⁱ USDA-ARS, Global Change and Photosynthesis Research Unit, Urbana, IL, United States

^j School of Natural Resources, University of Nebraska-Lincoln, Lincoln, Nebraska, United States

^k School of Agriculture and Environment, University of Western Australia, Crawley, WA, Australia

ARTICLE INFO

Keywords:

Cropland

Footprint

Gross primary productivity

Ground

Solar-induced chlorophyll fluorescence

ABSTRACT

Ground solar-induced chlorophyll fluorescence (SIF) is important for the mechanistic understanding of the dynamics of vegetation gross primary production (GPP) at fine spatiotemporal scales. However, eddy covariance (EC) observations generally cover larger footprint areas than ground SIF observations (a bare fiber with nadir), and this footprint mismatch between nadir SIF and GPP could complicate the canopy SIF-GPP relationships. Here, we upscaled nadir SIF observations to EC footprint and investigated the change in SIF-GPP relationships after the upscaling in cropland. We included 13 site-years data in our study, with seven site-years corn, four site-years soybeans, and two site-years miscanthus, all located in the US Corn Belt. All sites' crop nadir SIF observations collected from the automated FluoSpec2 system (a hemispheric-nadir system) were upscaled to the GPP footprint-based SIF using vegetation indices (VIs) calculated from high spatiotemporal satellite reflectance data. We found that SIF-GPP relationships were not substantially changed after upscaling nadir SIF to GPP footprint at our crop sites planted with corn, soybean, and miscanthus, with R^2 change after the upscaling ranging from -0.007 to 0.051 and root mean square error (RMSE) difference from -0.658 to 0.095 $\mu\text{mol m}^{-2} \text{s}^{-1}$ relative to original nadir SIF-GPP relationships across all the site-years. The variation of the SIF-GPP relationship within each species across different site-years was similar between the original nadir SIF and upscaled SIF. Different VIs, EC footprint models, and satellite data led to marginal differences in the SIF-GPP relationships when upscaling nadir SIF to EC footprint. Our study provided a methodological framework to correct this spatial mismatch between ground nadir SIF and GPP observations for croplands and potentially for other ecosystems. Our results also demonstrated that the spatial mismatch between ground nadir SIF and GPP might not significantly affect the SIF-GPP relationship in cropland that are largely homogeneous.

1. Introduction

Accurate quantification of gross primary productivity (GPP) is

critical for studying the global carbon cycle and understanding terrestrial ecosystem dynamics (Jiang et al., 2020; Ryu et al., 2019). The eddy covariance (EC) technique has long been used to measure carbon fluxes

Abbreviations: GPP, Gross primary production; SIF, Solar-induced chlorophyll fluorescence.

* Corresponding authors.

E-mail addresses: wugh16@gmail.com (G. Wu), kaiyug@illinois.edu (K. Guan).

<https://doi.org/10.1016/j.agrformet.2023.109532>

Received 15 November 2022; Received in revised form 27 March 2023; Accepted 22 May 2023

Available online 27 May 2023

0168-1923/© 2023 Elsevier B.V. All rights reserved.

at the ecosystem scale (Baldocchi, 2003), but the distribution of EC sites is limited at regional to global scales (Baldocchi et al., 2001; Kumar et al., 2016). Recent progress in satellite solar-induced chlorophyll fluorescence (SIF) has provided a new opportunity for continuous regional to global terrestrial GPP estimation (Frankenberg et al., 2011; Li and Xiao, 2022; Sun et al., 2017). However, the coarse spatial resolution of the current satellite SIF dataset complicates the direct link between satellite SIF and EC GPP (Magney et al., 2020). Therefore, ground tower-based spectral systems for SIF observations concurrent with EC measurements have been used to better understand the relationship between SIF and GPP at the ecosystem scale (Miao et al., 2018; Wu et al., 2022b; Yang et al., 2015; Y. Zhang et al., 2021).

Over the last decade, several tower-based spectral systems for SIF measurements, which require high spectral resolution (full width at half maximum (FWHM) < 1 nm) and cover the SIF emission spectral range (650–850 nm), have been developed (e.g., Du et al., 2019; Grossmann et al., 2018; Gu et al., 2019; Yang et al., 2018). Tower-based spectral systems measure both downwelling solar irradiation and upwelling canopy radiance to retrieve SIF (Cendrero-Mateo et al., 2019; Meroni et al., 2009). The most common instrument designs are bi-hemispherical systems such as FAME (Gu et al., 2019) and SIFprism (Zhang et al., 2019), and hemispherical-conical systems, such as FluoSpec2 (Yang et al., 2018) and Photospec (Grossmann et al., 2018). Bi-hemispherical systems are equipped with a cosine-corrected foreoptic of the field of view (FOV) of 180° for canopy radiance collection. They sample a wide area, and their footprint is more comparable to the EC footprint, but the longer atmospheric radiation transfer path between canopy and foreoptic increases the uncertainty of SIF retrieval (Liu et al., 2017). Hemispherical-conical systems use a bare fiber with a small FOV (typically 25°) pointed at nadir or off-nadir for radiance acquisition, and their sample area covers only a small portion of the EC footprint (~2%, Fig. 1). Additionally, the EC footprint is temporally and spatially varying with turbulent conditions and wind direction (Foken and Leclerc, 2004; Rannik et al., 2012), while spectral observations from both bi-hemispherical and hemispherical-conical systems with fixed view zenith angles always sample the same area (Fig. 1). This sampling area mismatch between SIF and GPP measurements could cause additional uncertainty for understanding SIF-GPP relationships as well as investigating the effect of canopy structure (e.g., Dechant et al., 2020; Li et al., 2020), leaf physiology (e.g., Wu et al., 2022a; Yang et al., 2021) and environmental conditions (e.g., Paul-Limoges et al., 2018) on SIF-GPP relationships.

Following the light use efficiency framework, observed canopy SIF can be decomposed into four components: photosynthetic active radiation (PAR), the fraction of absorbed PAR of the canopy (FPAR), fluorescence emission yield of the canopy ($\Phi_{F, \text{canopy}}$), and the fraction of SIF photons escaped from the canopy due to scattering and reabsorption

within the canopy (f_{esc}) (Frankenberg and Berry, 2018):

$$\text{SIF} = \text{PAR} \times \text{FPAR} \times \Phi_{F, \text{canopy}} \times f_{\text{esc}}, \quad (1)$$

Previous studies have found the dominant roles of structural (FPAR, f_{esc}) and radiation components (PAR) in SIF signals across various ecosystems (e.g., Dechant et al., 2020; Miao et al., 2018). Strong correlations between SIF and vegetation indices (VIs) which mainly captures the structural information of vegetation such as near-infrared reflectance of vegetation (NIRv) and enhanced vegetation index (EVI) have been reported at weekly (Doughty et al., 2021) to monthly scales (Badgley et al., 2017). At short time scales when the contribution of PAR to SIF is important, the product of NIRv and PAR (NIRvP) has been shown to be a strong proxy for SIF at different spatial scales (Dechant et al., 2022). Many studies have utilized VIs, surface reflectance, and radiation information from Moderate Resolution Imaging Spectroradiometer (MODIS) to downscale coarse satellite SIF products to moderate spatial (e.g., 0.05°) and temporal SIF (e.g., 8 days and 16 days) products with various statistical methods (Duveiller et al., 2020; Turner et al., 2020; Wen et al., 2020; Yu et al., 2018).

New-generation satellite surface reflectance data with high-spatial-and-temporal-resolution such as Planetscope (PS) and Sentinel-2 (S2) provide a new opportunity to upscale ground SIF observations with a small coverage to the whole EC footprint. PS sensors installed on constellations of nanosatellites are able to provide near-daily visible to near-infrared band reflectance at a 3 m spatial resolution across the globe (Houborg and McCabe, 2016). S2 sensors offer images at 10–20 m spatial resolutions at the visible, red-edge and near-infrared bands with a global average 5-day revisit time (Immitzer et al., 2016). Surface reflectance and calculated VIs from PS and/or S2 have been used in various ecological applications such as land cover classification (Mashonganyika et al., 2021; Mudereri et al., 2019), aboveground carbon stock estimation (Baloloy et al., 2018; Csillik et al., 2019) and crop growth monitoring (Kamenova and Dimitrov, 2021; Kimm et al., 2020; Sadeh et al., 2021). Considering the important role of structural information in SIF signals, VIs calculated from these high spatiotemporal resolution data can be utilized as a bridge to match the sampling area of SIF and GPP which could potentially decrease the uncertainty of SIF-GPP relationships.

In this paper, we aim to upscale ground canopy SIF from a small sampling area to match the EC footprint using PS and S2 at multiple cropland sites from 2017 to 2021, and then investigate the change in SIF-GPP relationships after this correction. These cropland sites are either planted with corn, soybean, or miscanthus located in the U.S. Corn Belt. Corn and soybean are among the most important annual row crops worldwide, and they are widely used as livestock feed, human food, biofuels, and raw materials in industry. Miscanthus is a warm-season, perennial grass, and it has tremendous potential for bioenergy

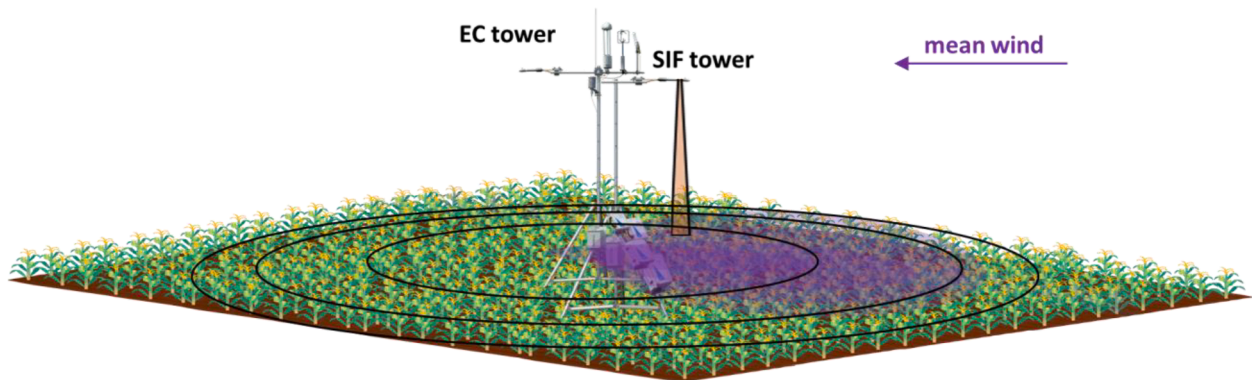


Fig. 1. Conceptual diagram illustrating the footprint mismatch between eddy covariance (EC) flux and nadir SIF observations. The orange area indicates the small nadir footprint (25° of FOV) of SIF observations. Black contours represent EC flux footprint climatologies. The purple area over the plants represents one specific half-hourly EC flux footprint with that half-hourly mean wind direction.

production (Heaton et al., 2010). Its significant carbon sequestration, high yield, high water and nutrient use efficiencies, non-invasiveness, and ability to grow on marginal land have sparked significant interest among researchers (Whitaker et al., 2018). Investigating the effect of upscaling ground nadir SIF to EC footprint on SIF-GPP relationships in these crops could improve our understanding of SIF as a proxy of GPP in both annual and perennial crops. We hypothesize that SIF-GPP relationships would be improved after matching the SIF and GPP sampling areas. Specifically, we hypothesized that after the correction, (1) the R^2 of the SIF-GPP relationship at each site-year as well as within each species would increase; (2) the regression slope and/or intercept within each species would be more convergent across different site-years. Additionally, considering that cropland sites are relatively homogeneous compared to natural ecosystems, we further hypothesize that the improvement of the SIF-GPP relationship after the SIF footprint upscaling would not be substantial.

2. Materials and methods

2.1. In situ data

2.1.1. Study sites

In-situ data from seven sites located in the U.S. Corn Belt from 2017 to 2021 (a total of 13 site-years) were used in this study. Two of the sites (US-Ne2 and US-Ne3) were located at the Eastern Nebraska Research and Extension Center of the University of Nebraska-Lincoln in Nebraska. Another five sites were all located in Illinois, with two sites (US-UiB and US-UiC) at the Energy Farm of the University of Illinois at Urbana-Champaign, and the other three sites (Reifsteck, Rund, and Reinhart) at the private farms in Champaign County. US-Ne2 was irrigated, and the other six sites were rainfed. Except for US-UiB which was always planted with miscanthus (mis), the other sites were either corn-soybean (soy) rotation or corn-corn-soy rotation. In-situ data from seven site-years for corn, four site-years for soybeans, and two site-years for miscanthus were collected. Corn and soybean were planted in April or May and harvested in September or October, and miscanthus emerged in April and was harvested in March of the next year. Detailed site and data availability information was summarized in Table 1.

Table 1

Site and SIF observation information. GPP data are available for the whole growing season for each site-year, except that at the Rund site in 2021 corn, GPP data from June to July is not available due to sensor failure. Soy: Soybean, Mis: Miscanthus.

Site	lat/lon	Year	Crop	Growing season	SIF
US-Ne2	41.1649°N/ 96.4701°W	2017	Corn	May 8 – Oct 30	Jul 15 – Oct 15
		2018	Soy	May 14 – Oct 19	Jun 19 – Oct 14
US-Ne3	41.1797°N/ 96.4397°W	2017	Corn	May 8 – Oct 30	Jul 15 – Oct 15
		2018	Soy	May 14 – Oct 19	Jul 8 – Oct 14
US-UiB	40.0628°N/ 88.1984°W	2019	Mis	Apr 2019 – Mar 2020	May 9 – Nov 19
		2020	Mis	Apr 2020 – Mar 2021	May 11 – Nov 1
US-UiC	40.0647°N/ 88.1983°W	2017	Corn	May 16 – Nov 2	Jun 7 – Oct 29
		2018	Corn	May 8 – Oct 9	Jun 28 – Oct 10
Reifsteck	39.8824°N/ 88.1546°W	2019	Soy	May 17 – Oct 9	Jun 5 – Oct 6
		2020	Soy	Apr 21 – Oct 3	May 2 – Oct 2
		2021	Corn	May 1 – Sep 26	May 16 – Sep 11
Rund	40.0070°N/ 88.2897°W	2021	Corn	Apr 26 – Dec 2	May 30 – Sep 18
Reinhart	39.8887°N/ 88.2140°W	2021	Corn	Apr 23 – Sep 25	May 15 – Sep 21

2.1.2. Stationary spectral measurements and SIF derivation

A hemispherical-conical system, FluoSpec2 (Miao et al., 2018; Yang et al., 2018), was installed at each site-year to collect spectral data. Two subsystems were included in FluoSpec2. One for SIF retrieval with a QEPRO spectrometer (Ocean Optics Inc., FL, USA) covering 730–780 nm at an interval of 0.15 nm. The other is for VI calculation with an HR2000+ spectrometer (Ocean Optics Inc., FL, USA) covering 400–1100 nm at an interval of 1.1 nm. Each spectrometer collected data from two fibers, one fiber for downwelling solar irradiance and the other for upwelling canopy radiance. An inline shutter was installed between the spectrometer and fibers to switch between irradiance and radiance. A cosine corrector was connected to the bare fiber for hemispherical solar irradiance collection, and a bare fiber with a FOV of 25° pointed at nadir was used for canopy radiance acquisition. The spectrometer and the shutter were placed in a temperature-controlled box, and the end of the fibers was placed at a 5-m tower above the ground with a sampling area of 2.2 m in diameter on the ground. Spectra data were collected automatically at a 5-min time interval using the software, FluoSpec Manager (Yang et al., 2018). Far-red SIF at 760 nm was retrieved from measured irradiance and radiance using the improved Fraunhofer Line Depth (iFLD) approach (Alonso et al., 2008; Cendrero-Mateo et al., 2019). The 5-min interval far-red SIF data was averaged to half hourly intervals to match the frequency of EC data. More details about the FluoSpec2 measurement sequence and SIF retrieval can be found in Wu et al. (2020).

2.1.3. Eddy covariance, meteorological and ground auxiliary measurements

EC and meteorological data were acquired from the EC and meteorological towers located in the same field as the FluoSpec2 system. Each EC system was equipped with a CO₂/H₂O infrared gas analyzer and a three-dimensional ultrasonic anemometer. Raw EC data recorded at 10 Hz frequency were processed using EddyPro (v6.2.0; LICOR Biosciences, NE, USA) to derive half-hourly net ecosystem exchange (NEE), sensible heat (H), latent heat (LE), friction velocity (u^*) and Obukhov length (L). EddyPro applied flux de-trending (block average), coordinate alignment (double rotation), time-lag compensation (covariance maximization), flux density correction (Webb–Pearman–Leuning, Webb et al., 1980), spikes detection and removal (Vickers and Mahrt, 1997). Meteorological variables such as air temperature (Ta), relative humidity (RH), incoming radiation, and reflected radiation were collected close to the EC systems at each site. Canopy height (h_c) was measured bi-weekly at each site-year using a ruler and/or tape measure. For US-Ne2 and US-Ne3 sites, the measurement height of EC instruments (z_m) was kept at 3 m for soybeans across the whole growing season, and for corn, it was at 3 m when h_c was lower than 1 m and increased to 6 m when h_c increased until the end of the growing season. For the US-UiB site and US-UiC site planted with corn, z_m was kept at ~3 m at the beginning of the growing season and increased to ~4.2 m with the increase of h_c . For the US-UiC and Reifsteck sites planted with soybean, z_m was at 2.6 and 3 m across the whole growing season, respectively. For the Reifsteck site planted with corn, Rund and Reinhart site, z_m was kept at around 4.8 m the whole time. Detailed information about the EC and meteorological tower instrumentation can be found in Suyker and Verma (2012) for US-Ne2 and US-Ne3 sites, and in Moore et al. (2020) for US-UiB and US-UiC sites.

EddyPro-processed NEE data further went through the quality assurance and quality control (QA/QC) to remove spikes and outliers, u^* filtering to exclude data from low turbulent conditions, gap-filling to acquire continuous half-hourly NEE, and flux partitioning to derive half-hourly GPP and ecosystem respiration (ER). For US-UiB and US-UiC sites, NEE data were removed when more than 50% of the data occurred outside of the targeted field due to the relatively small field size (200 m × 200 m). The ONEFlux processing pipeline which followed the standard FLUXNET2015 protocol was used to process the Eddypro-processed EC data at each site. More details about the ONEFlux

pipeline can be found in Pastorello et al. (2020).

2.2. Satellite reflectance data

2.2.1. Sentinel-2

We derived daily 10m-resolution surface reflectance data from publicly available Sentinel-2 satellite images. Sentinel-2 L1C top of atmosphere reflectance data and L2A surface reflectance data were obtained before and after 2019, respectively. The official data processing tool Sen2Cor was employed to conduct an atmospheric correction and spatial resampling. Sentinel-2 Scene Classification (SCL) was used to remove pixels other than “Vegetation”, “Bare Soils” and “Water”. Non-water pixels with blue reflectance larger than 0.4 or near-infrared reflectance smaller than visible reflectance were considered cloud-contaminated pixels and thus removed. We further applied a temporal filter to remove outliers, assuming that surface reflectance should vary smoothly within a certain time period. For a specific day, we utilized a 15 day-radius temporally moving window from which the mean and standard deviation of the time series were calculated. Reflectance values outside the range of mean ± 1.5 standard deviations were considered outliers and dropped. Subsequently, the mean of the first 15 days and that of the last 15 days were calculated, respectively. If the reflectance value of the target day was 50% smaller or larger than both the first 15 days’ mean and the last 15 days’ mean, that reflectance value was considered an outlier and dropped. After outliers’ removal, we applied a temporal filter to interpolate and smooth data. Similar to the outlier removal step, a temporally moving window with a one-month radius was utilized for a specific day. A Gaussian filter was used to calculate the weighted sum of the time series reflectance, with larger weights assigned to close days and smaller weights assigned to distant days. The Gaussian filter was applied every day so that a smoothed gap-free daily 10 m surface reflectance dataset was derived.

2.2.2. PlanetScope

We derived daily 3m-resolution surface reflectance data from commercial PlanetScope satellite images. PlanetScope 4-band (blue, green, red, and near-infrared) surface reflectance swath data were used as the data source. To reduce between-swath difference and day-to-day variation caused by different overpass times and viewing angles, a cumulative distribution function (CDF) matching procedure was employed. We used the MCD43A4 daily 500m-resolution MODIS Nadir BRDF-Adjusted Reflectance (NBAR) product as a benchmark. For each PlanetScope swath image, the MODIS image over the same area was cropped and resampled to a 3 m resolution. Quality control information from both PlanetScope data and MODIS data was used to remove clouds. For each band, cumulated histograms were built for both cloud-free PlanetScope and MODIS images, and linear interpolation was used to determine updated values of PlanetScope surface reflectance that correspond most closely to the MODIS surface reflectance values. After the CDF matching, outlier detection and Gaussian interpolation/smoothing procedure were applied to derive daily data, similar to Sentinel-2.

2.3. Correcting ground SIF to EC footprint-based SIF

2.3.1. Method overview

Considering the importance of structural components in SIF signals, we would expect the product of VI and PAR to explain the majority of SIF signals. Therefore, VI calculated from high spatiotemporal PS, and S2 reflectance data could be used to upscale observed SIF from the small sampling area to the whole EC footprint. Specifically, we first selected the proper VI based on the relationship between SIF and the product of VI and PAR from portable spectral campaigns (Section 2.3.2). Next, we calculated the half-hourly EC footprint using two footprint models (Section 2.3.3), and further calculated EC footprint weighted VI from PS and S2 ($VI_{EC\ footprint}$, Eq. (2)). VI of the SIF sampling area (\sim diameter 2.2

m on the ground) was represented by a single $3\text{ m} \times 3\text{ m}$ pixel VI of PS or a single $10\text{ m} \times 10\text{ m}$ VI of S2 imagery covering the SIF tower ($VI_{SIF\ pixel}$). Finally, the ratio of half-hourly $VI_{EC\ footprint}$ to daily $VI_{SIF\ pixel}$ was estimated (Eq. (3)) and this ratio was multiplied by observed half-hourly SIF (SIF_{obs}) to derive half-hourly EC footprint-based SIF ($SIF_{EC\ footprint}$, Eq. (4)) with the assumption that PAR was the same between EC footprint and SIF sampling area (i.e. $PAR_{EC\ footprint} \approx PAR_{SIF\ pixel}$). Different satellite reflectance data and EC footprint models were used to investigate whether the sources of data and EC footprint model would impact the correction results.

$$VI_{EC\ footprint} = \sum_{i=1}^N w_i \times VI_i, \quad (2)$$

$$Ratio_{EC\ footprint, SIF\ pixel} = \frac{VI_{EC\ footprint} \times PAR_{EC\ footprint}}{VI_{SIF\ pixel} \times PAR_{SIF\ pixel}} \approx \frac{VI_{EC\ footprint}}{VI_{SIF\ pixel}}, \quad (3)$$

$$SIF_{EC\ footprint} = SIF_{obs} \times Ratio_{EC\ footprint, SIF\ pixel}, \quad (4)$$

where $VI_{EC\ footprint}$ was calculated by the sum of the product of VI (VI_i) and footprint weight (w_i) at each pixel i across all the pixels within the EC footprint N . For the US-UiB and US-UiC sites, the EC footprint was constrained by the field boundary, and only the footprint within the target field was used to calculate $VI_{EC\ footprint}$ and $Ratio_{EC\ footprint, SIF\ pixel}$.

2.3.2. VI selection from the portable spectral campaign and daily VI from PS and S2

Portable spectral campaigns were conducted in the 2021 growing season to investigate the relationship between SIF and the product of different VI and PAR in corn and soybean in Champaign County, Illinois. Two corn sites (Rund and Reinhart) and two soybean sites at the Energy Farm of the University of Illinois at Urbana-Champaign were included. For each site, spectral data from 20 essential sample units (ESU), each with a size of about $2 \times 2\text{ m}$ (Fig. S1), were collected at a time interval of 2–4 weeks. The spectral system used for portable campaigns had the same instrumentation setup as FluoSpec2 except that a single fiber was used to collect both downwelling irradiance and upwelling radiance for each subsystem. We measured downwelling irradiance by pointing bare fibers at a leveled standard reflection board (Spectralon®; Labsphere, NH, USA) and upwelling radiance by pointing at the canopy with a nadir view. At each ESU, a total of 20 points were measured, and the average of 20 irradiances and radiances from the QEPRO spectrometer were used to retrieve SIF at 760 nm at each ESU using the iFLD method. Different VIs were calculated from the HR2000+ reflectance. PAR at each ESU was estimated by integrating HR2000+ downwelling irradiance from 400 to 700 nm. Compared to the stationary spectral measurements (Section 2.1.2), this portable campaign included the spatial relationships between SIF and the product of VIs and PAR within each site, which was essential for the upscaling of SIF from a single pixel to the whole EC footprint for each site-year.

Five common VIs used in corn and soybean were investigated (Table S1). NIRv and EVI are strongly correlated with SIF (Badgley et al., 2017; Dechant et al., 2022; Doughty et al., 2021), and Normalized Difference Vegetation Index (NDVI), Red edge NDVI (NDVI_{rededge}) and Green NDVI (NDVI_{green}) are proxies of FPAR in corn and soybean (Thenkabail et al., 2011). The results showed that across spatiotemporal scales, the product of EVI and PAR and the product of NIRv and PAR showed a stronger correlation with SIF compared to NDVI and NDVI_{green} (Fig. 2; Fig. S2). This strong correlation was not affected by sun angles (Fig. S3). They explained no less than 85% and 94% percent of SIF variation in corn and soybean, respectively (Fig. 2). The product of NDVI_{rededge} and PAR also showed strong correlation with SIF. However, NDVI_{rededge} can only be calculated from S2 reflectance data due to the missing red edge band in PS reflectance data. Therefore, daily EVI and NIRv calculated from daily PS and S2 reflectance were used to upscale stationary observed SIF to EC footprint-based SIF.

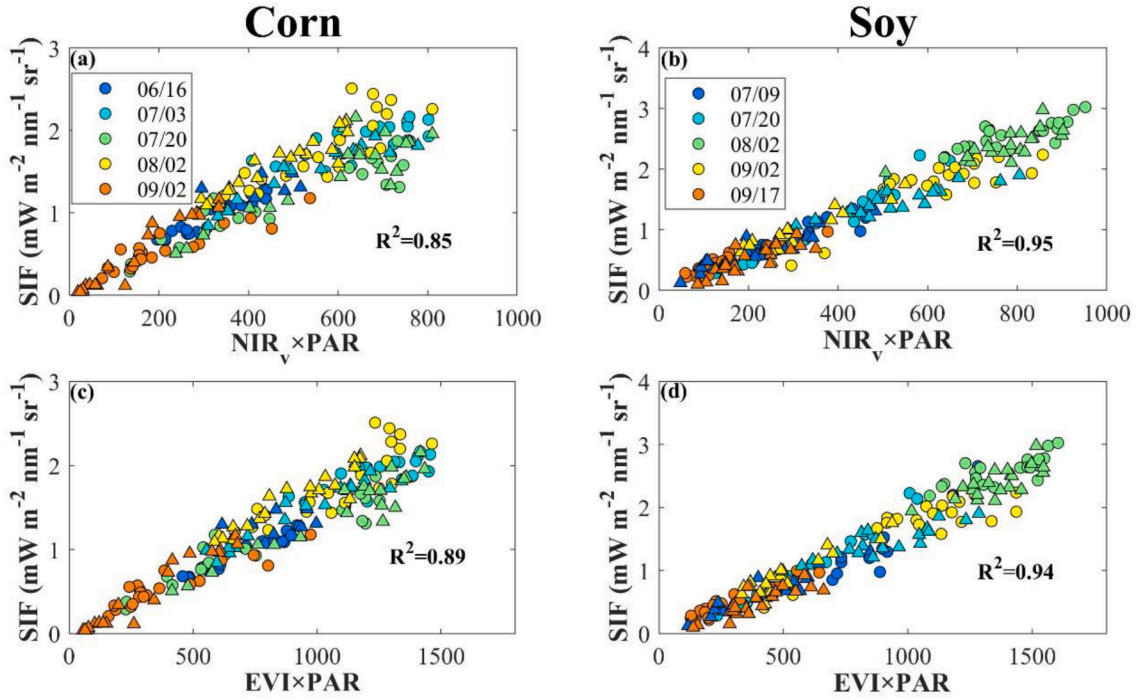


Fig. 2. The relationship between nadir-view SIF and the product of NIRv and PAR, and between SIF and the product of EVI and PAR in corn (left) and soybean (right) from the 2021 portable campaign. Different colors represent different dates (mm/dd) and different symbols (filled circles and triangles) represent different sites.

$$NIR_v = \rho_{NIR} \times \frac{\rho_{NIR} - \rho_{RED}}{\rho_{NIR} + \rho_{RED}}, \quad (5)$$

$$EVI = 2.5 \times \frac{\rho_{NIR} - \rho_{RED}}{\rho_{NIR} + 6 \times \rho_{RED} + 7.5 \times \rho_{BLUE} + 1}, \quad (6)$$

where ρ_{NIR} , ρ_{RED} and ρ_{BLUE} were PS or S2 surface reflectance at near-infrared band, red band, and blue band, respectively. For PS, the central wavelengths for blue, red, and near-infrared bands were 490 nm, 665 nm, and 865 nm, respectively, and for S2, they were 492 nm, 665 nm, and 833 nm, respectively. To minimize the effect of soil background on NIRv and EVI, soil adjusted NIRv (SANIRv) and soil adjusted EVI (SAEVI) were calculated following the method proposed by Jiang et al. (2020):

$$SANIR_v = \frac{NIR_v - NIR_{v, soil}}{NIR_{v, peak} - NIR_{v, soil}} \times NIR_{v, peak}, \quad (7)$$

$$SAEVI = \frac{EVI - EVI_{soil}}{EVI_{peak} - EVI_{soil}} \times EVI_{peak}, \quad (8)$$

where $NIR_{v, peak}$ and EVI_{peak} are the maximum value of the multi-year average NIRv and EVI time series on a per-pixel basis, respectively; $NIR_{v, soil}$ and EVI_{soil} are the soil background NIRv and EVI derived from the multi-year average NIRv and EVI time series per pixel, respectively. SANIRv and SAEVI did not change the peak of NIRv and EVI but changed for low NIRv and EVI values. SANIRv and EVI were set 0 when NIRv and EVI were lower than $NIR_{v, soil}$ and EVI_{soil} .

2.3.3. EC flux footprint calculation for each site-year

Two different EC flux footprint models were used to calculate half-hourly footprint weights within 1 km of the EC tower. One was the Flux Footprint Prediction (FFP) model (<http://footprint.kljun.net/>) developed by (Kljun et al., 2015), and the other one was the Simple Analytical Footprint model on Eulerian coordinates (SAFE) developed by Chen et al. (2009) based on the formulation of Kormann and Meixner (2001). The inputs for the FFP model included measurement height above displacement height (z), roughness length (z_0), mean wind speed

(u_{mean}), wind direction (w_{dir}), boundary layer height (blh), the standard deviation of lateral velocity fluctuations (σ_{lav}), L and u^* . The inputs for the SAFE model were above canopy T_a , RH, LE, H, NEE, u^* , z_m , u_{mean} , w_{dir} , σ_{lav} , air pressure (Pa). z_m for the SAFE model was the recorded EC instrument height. z for FFP was calculated by the difference between z_m and the displacement height which was approximated by 0.67 times canopy height h_c (Maurer et al., 2015). z_0 was estimated as 0.10 times h_c (Raupach, 1994). Canopy heights were linearly interpolated to acquire half-hourly values. u_{mean} , w_{dir} , σ_{lav} , L , u^* , LE, H and NEE were output from EddyPro. T_a and RH were from the meteorological tower. Hourly blh for the FFP model at each site-year was downloaded from a high-resolution reanalysis product (ERA5) generated by the European Center for Medium-Range Weather Forecasts (ECMWF) at a 0.25° resolution (Y. Zhang et al., 2020) and linearly interpolated to half-hourly scale. When combined with PS derived-VI to derive EC footprint weighted VI, FFP and SAFE models were run at 3 m resolution to acquire half-hourly footprint weights centered on the EC tower, and for S2 derived-VI, they were run at 10 m resolution.

2.4. Data analysis

To test our hypotheses, the relationship between SIF and GPP before and after the footprint correction was analyzed. Linear regression of GPP-SIF at a half-hourly scale was established for each site-year before and after the footprint correction separately. The change in R^2 and root mean squared error (RMSE) before and after the correction was used to evaluate the performance of footprint correction at each site-year. The standard deviations of regression slope and intercept of the same species across different site-years after and before the correction were also computed. The Tukey test was used to investigate where the regression slope and intercept were significantly different before and after footprint correction. Additionally, for each species, we combined the data from all site-years and built SIF-GPP relationships before and after the correction to investigate the overall change in the SIF-GPP relationship for each species. Considering the uncertainties of SIF under low light conditions in the early morning and late afternoon, only data from 8:00 am to 6:00 pm (local standard time) were used. Since we considered two satellite

sources (PS and S2), four VIs (NIRv, EVI, SANIRv, SAEVI), and two EC footprint models (FFP and SAFE), a total of 16 cases were included. The PS-based results (8 cases) are presented in the main text, and S2-based results are shown in the appendix and supplementary materials.

3. Results

3.1. EC footprint and evaluation of spatial heterogeneity at each site-year

Overall, the field conditions were relatively homogeneous at our crop sites. Across all the site-years, the maximal distance from the EC tower to the 90% contour of the daytime July footprint climatologies calculated from the SAFE model ranged from ~100 m to 400 m (Fig. 3). EC footprints calculated from the FFP model covered a smaller area (the maximal distance from the tower to the 90% contour ranged from 50 m to 100 m) compared to the SAFE model footprint (Fig. S3). The half-hourly ratio of EC footprint weighted PS VI $VI_{EC\ footprint}$ (NIRv and EVI) to SIF tower pixel PS VI $VI_{SIF\ pixel}$ (NIRv and EVI) calculated from both EC footprint models ranged from 0.80 to 1.33, with mean 1.02 (Fig. 4), indicating that the field conditions were homogenous across the site years. The ratio calculated from the SAFE model (maximum ratio 1.33) was slightly higher than that calculated from the FFP model (maximum ratio 1.21) (Fig. 4). Soil adjusted VI (SANIRv and SAEVI)-based ratio showed larger variations at the early and late growing season compared to VI-based ratio (Fig. S5). S2 VI-based ratio ranged from 0.21 to 1.99 with a mean 1.04. Overall, the S2-based ratio showed similar seasonal variations, but a larger range compared to the PS-based ratio at most site-years except the US-Ne3 2017, US-UiC 2017, Reinhart 2021, and Reifsteck 2020 where the S2-based ratio was substantially higher at the early and end of the growing season (Fig. S6 & S7).

3.2. The change of SIF-GPP relationships after footprint correction at each site-year

SIF-GPP relationships were not considerably improved after upscaling the nadir SIF to EC footprint-based SIF, with the R^2 and RMSE difference before and after correction among all the PS-based ratio cases ranging from -0.007 to 0.051 and from -0.658 to $0.095\ \mu\text{mol}\ m^{-2}\ s^{-1}$ across all the site-years at the half-hourly timestamp, respectively (Figs. 5 and 6). At daily scale, R^2 difference ranged from -0.009 to 0.061 (Fig. S8) and RMSE difference ranged from -0.710 to $0.129\ \mu\text{mol}\ m^{-2}\ s^{-1}$ among all the PS-based cases across all the site-years (Fig. S9). Except for US-Ne2 2017 and US-UiC 2018 where R^2 decreased, and RMSE increased after correction in most cases, the S2-based ratio showed similar results as the PS-based ratio, with the R^2 and RMSE difference ranging from -0.017 to 0.066 and from -0.869 to 0.215 , respectively (Figs. A1 and A2). The largest improvement in SIF-GPP relationships was observed at the US-Ne2 2018 soybean site. Among all the PS-based ratio cases, the ratio calculated from soil adjusted VI (SANIRv and SAEVI) and SAFE footprint showed a slightly larger R^2 increase compared to other ratio cases for most site-years. For corn, SIF footprint upscaling did not decrease the variation of the SIF-GPP relationships across different site-years, indicated by the similar standard deviation of the linear regression slope and intercept between original nadir SIF and upscaled EC footprint SIF (Fig. 7a, d). For soybean, the standard deviation of regression intercept of SIF-GPP decreased after nadir SIF footprint upscaling, but not significantly (Fig. 7b, e). For miscanthus, matching SIF and GPP footprints did not decrease the interannual variation of the SIF-GPP relationships, but the regression slope declined after the SIF footprint upscaling, but not significantly (Fig. 7c, f). Those results about regression slopes and intercepts were consistent between PS-based ratio cases and S2-based ratio cases for corn and soybean, but for miscanthus, SIF footprint upscaling increased the variation of SIF-GPP relationships between two years (Fig. A3). Among all the PS-based ratio cases, the ratio calculated from SAEVI, and SAFE model

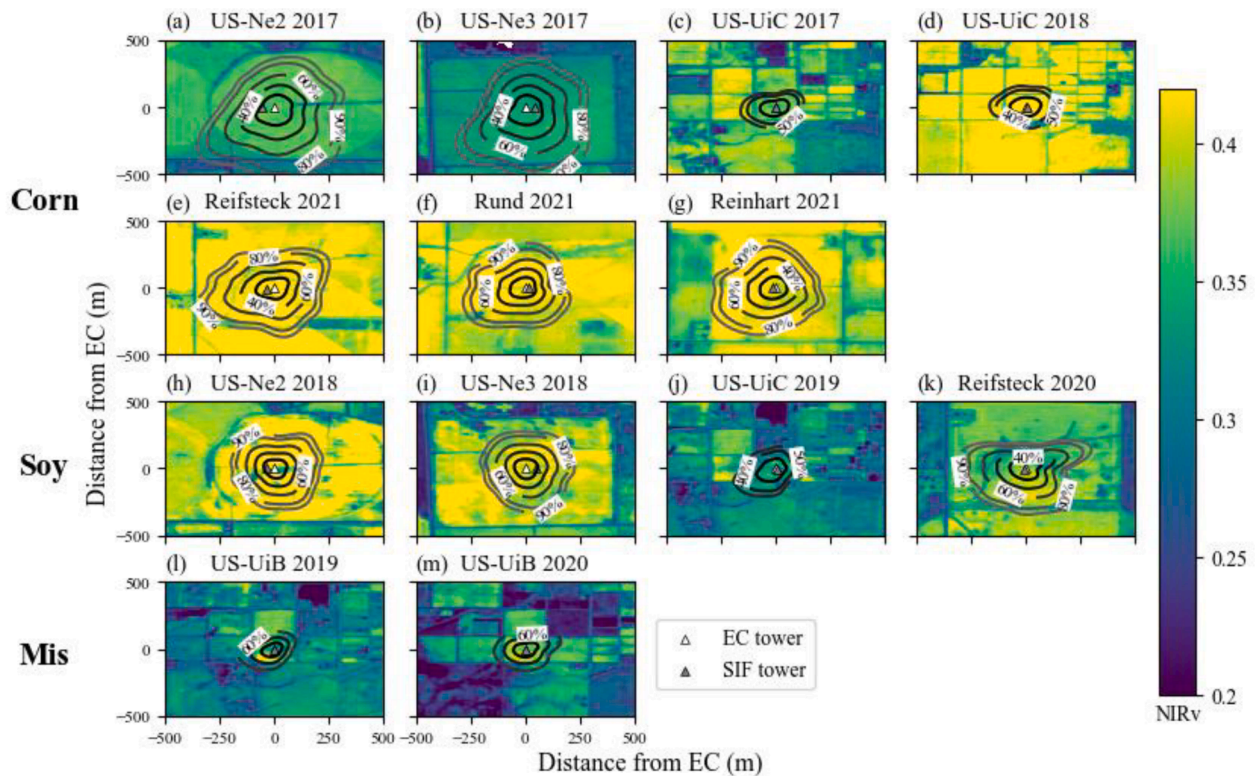


Fig. 3. Climatology of daytime (8 am to 6 pm) footprints in July calculated by the SAFE model. Background is PS NIRv on July, 15th at each site-year. The blank triangle and gray triangle indicate the location of the SIF tower and EC tower, respectively.

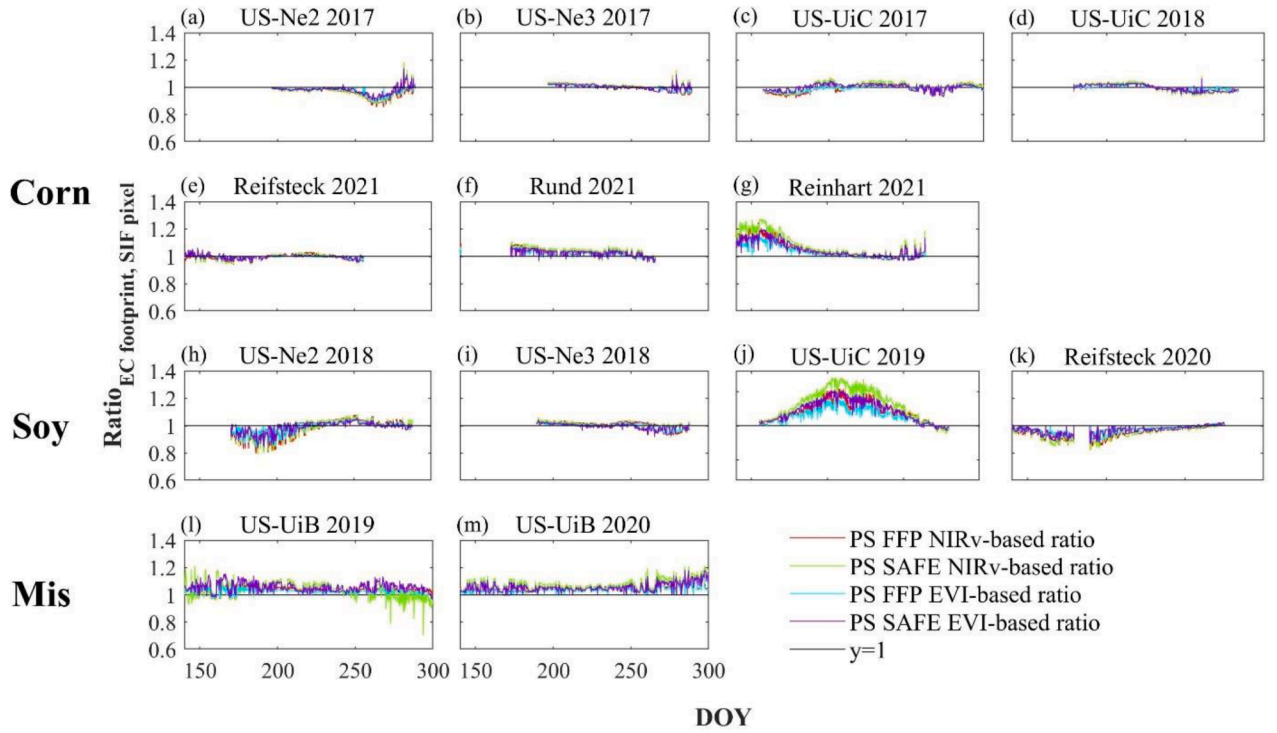


Fig. 4. The ratio of EC footprint weighted VI $VI_{EC\ footprint}$ and SIF pixel VI $VI_{SIF\ pixel}$ at each site-year (a-m). Different colors represent 4 different cases using PS data, two EC footprint models (FFP and SAFE) and two VIs (NIRv and EVI). The black line in each sub-figure represents that the ratio equals 1.

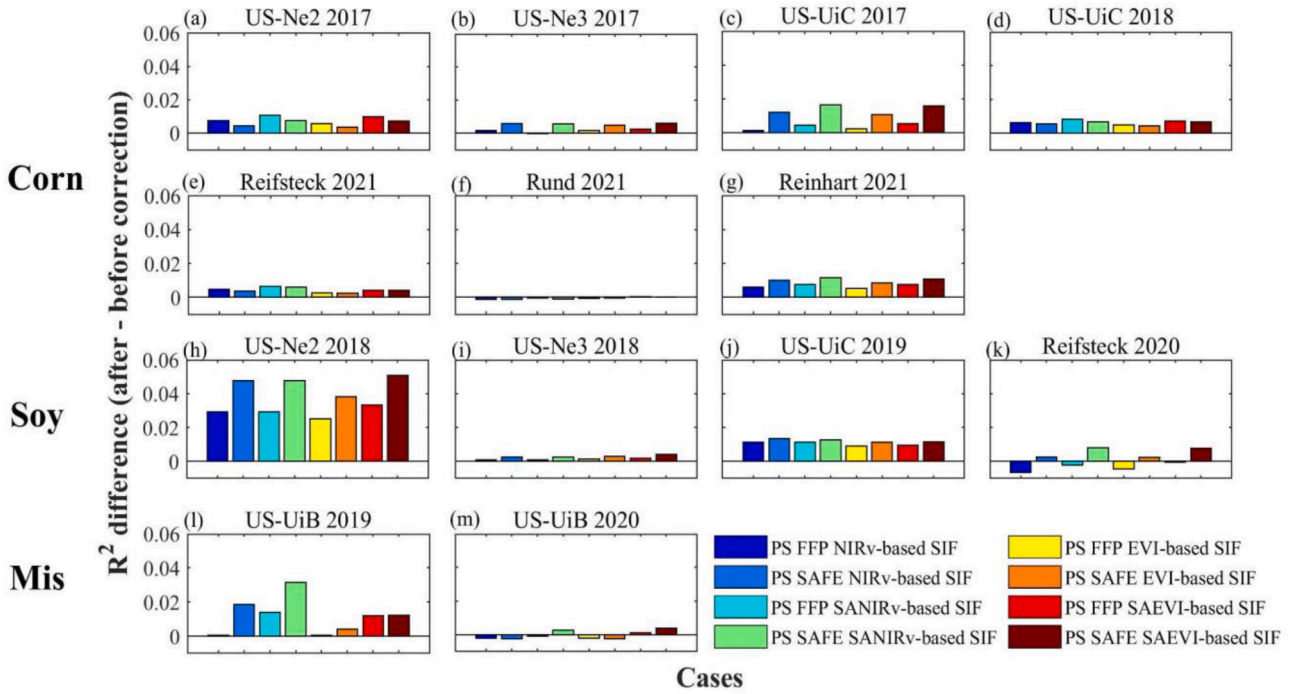


Fig. 5. The change of R^2 of the SIF-GPP relationship at the half-hourly timestamp after the footprint correction at each site-year. Different colors represent 8 different cases using PS data, two EC footprint models (FFP and SAFE), and four VIs (NIRv, SANIRv, EVI, and SAEVI).

showed the largest decrease in the standard deviation of regression intercept in soybean and regression slope in miscanthus (Fig. 7c, e).

3.3. The change of SIF-GPP relationships after footprint correction for each species

For each species, the SIF-GPP relationship did not considerably change after matching the footprint between SIF and GPP in terms of R^2 , RMSE, linear regression slopes, and intercepts (Fig. 8 and A4). Among all

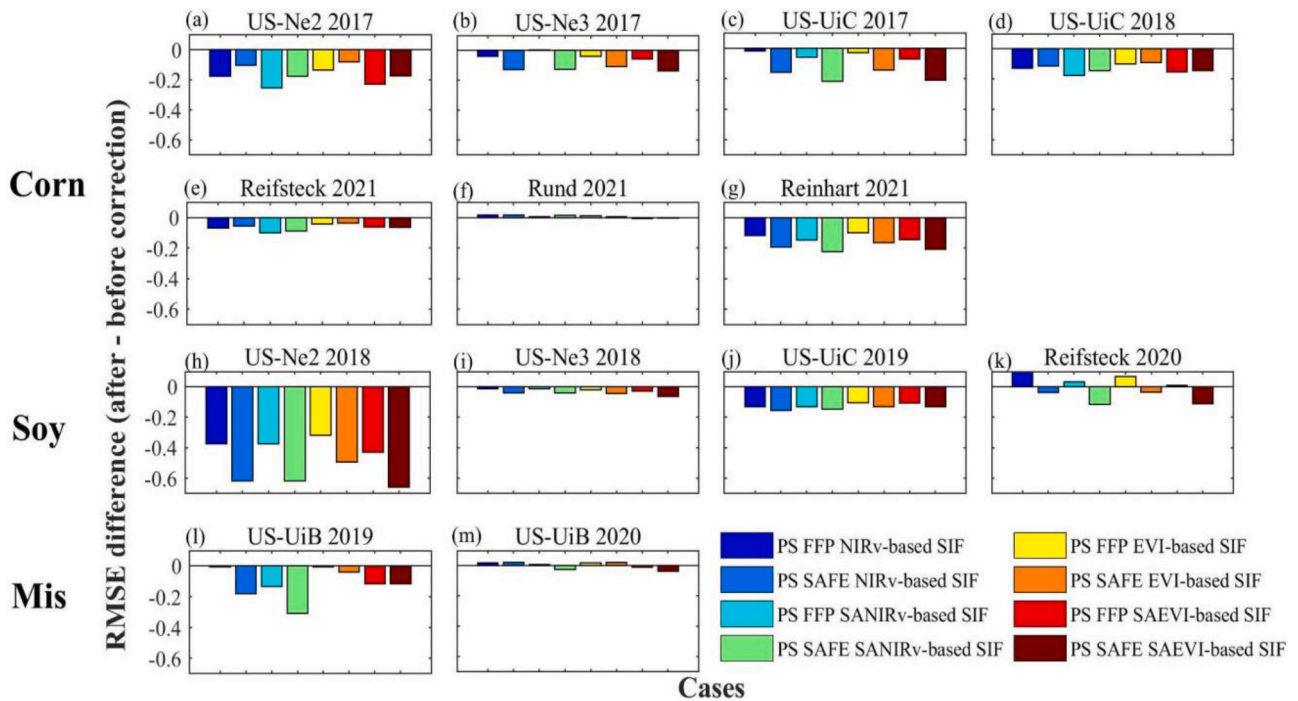


Fig. 6. The change of RMSE of the SIF-GPP relationship at the half-hourly timestamp after the footprint correction at each site-year. Different colors represent 8 different cases using PS data, two EC footprint models (FFP and SAFE), and four VIs (NIRv, SANIRv, EVI, and SAEVI).

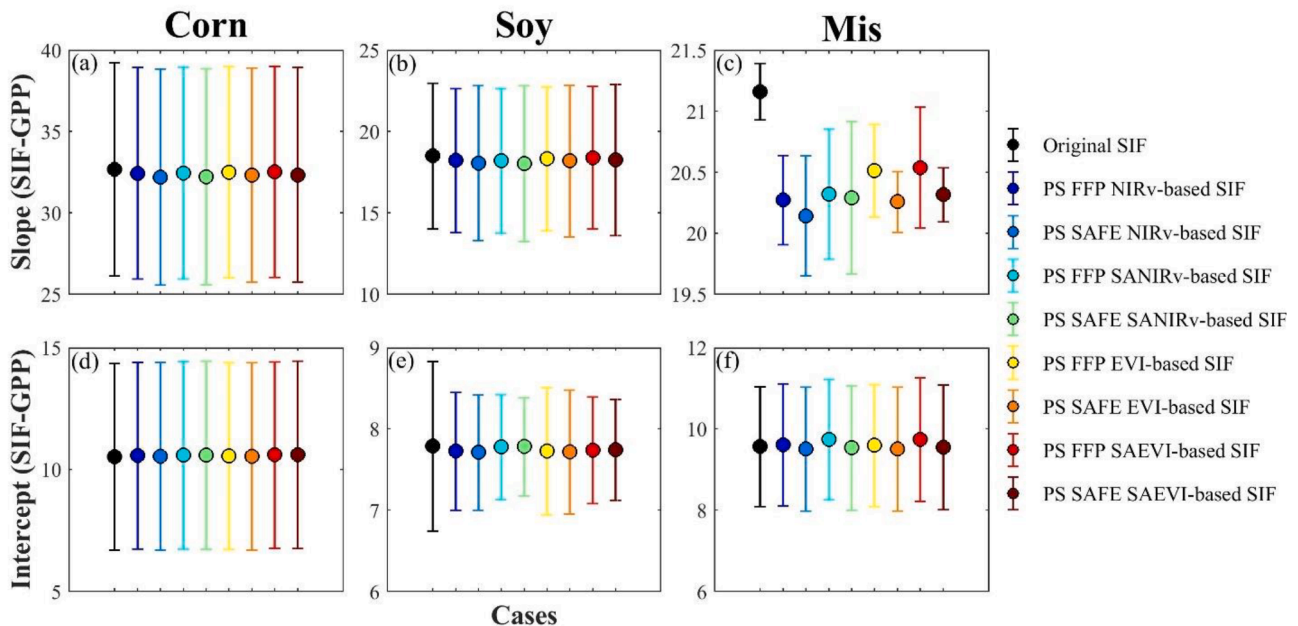


Fig. 7. The regression slope and intercept variation across different site-years within corn (a, d), soybean (b, e), and miscanthus (c, f) for the original SIF (black dots) and footprint corrected SIF (colored dots) using PS data, two EC footprint models (FFP and SAFE) and four VIs (NIRv, SANIRv, EVI, and SAEVI). Data shown are mean \pm standard deviation.

the PS-based ratio cases, the largest R^2 increases were 0.009, 0.012, and 0.019 for corn, soybean, and miscanthus, respectively. The largest RMSE decreases were 0.153, 0.148, and 0.183 for corn, soybean, and miscanthus, respectively. Among the S2-based ratio cases, the largest R^2 increases were 0.015, 0.007, and 0.014, respectively, but some S2-based ratio cases indeed degraded SIF-GPP relationships after nadir SIF footprint upscaling (Fig. A4). For corn and soybean, the PS-based ratio calculated from SAEVI showed the largest improvement in terms of R^2 . For miscanthus, the PS-based ratio calculated from SANIRv showed the

largest R^2 increase. The change of the linear regression slope of SIF-GPP ranged from -1.644 to 0.048 , from -0.879 to 0.421 , and from -1.955 to -1.0539 for corn, soybean, and miscanthus respectively, and the change of the regression intercept ranged from 0.051 to 0.414 , from -0.381 to 0.236 , from -0.183 to 0.065 , respectively. Corn SIF-GPP relationship showed the highest R^2 , and regression slope, followed by miscanthus and soybean, and nadir SIF footprint upscaling did not change this pattern (Fig. 9).

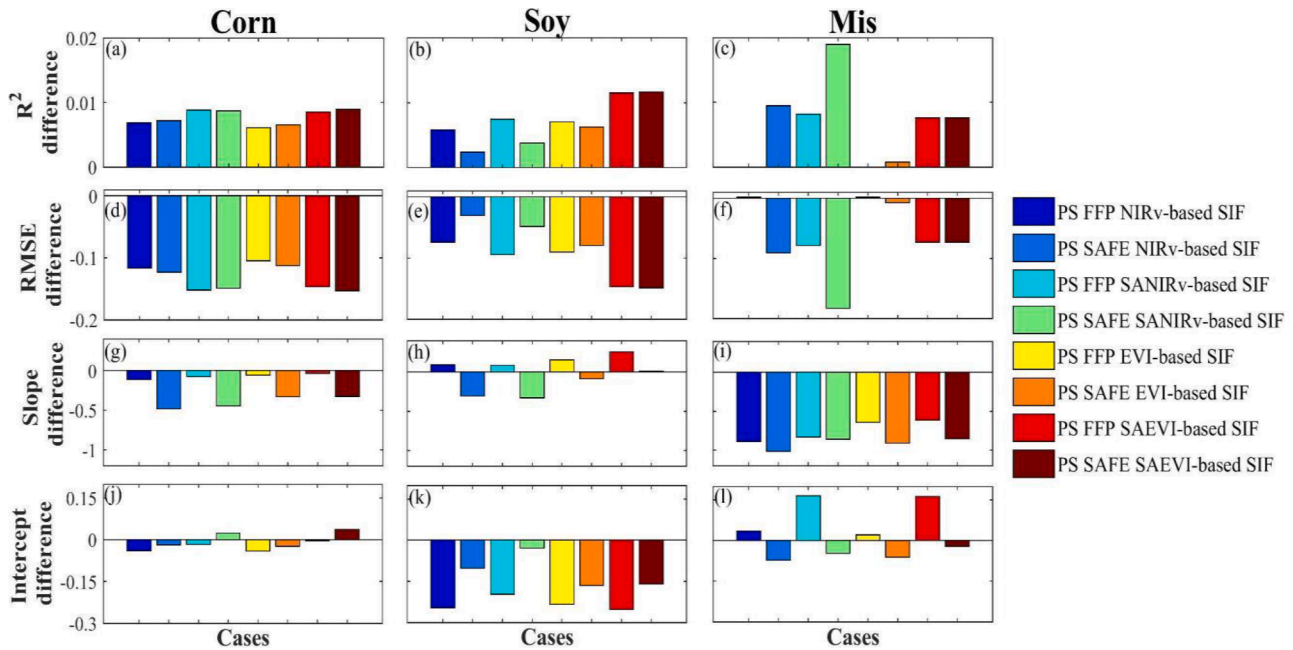


Fig. 8. The overall half-hourly SIF-GPP relationship change (R^2 , RMSE, regression slope, and intercept) after the footprint correction for each species when data from all site-years for the same species are combined. A total of 8 cases using PS data, two EC footprint models (FFP and SAFE), and four VIs (NIRv, SANIRv, EVI, and SAEVI) were considered.

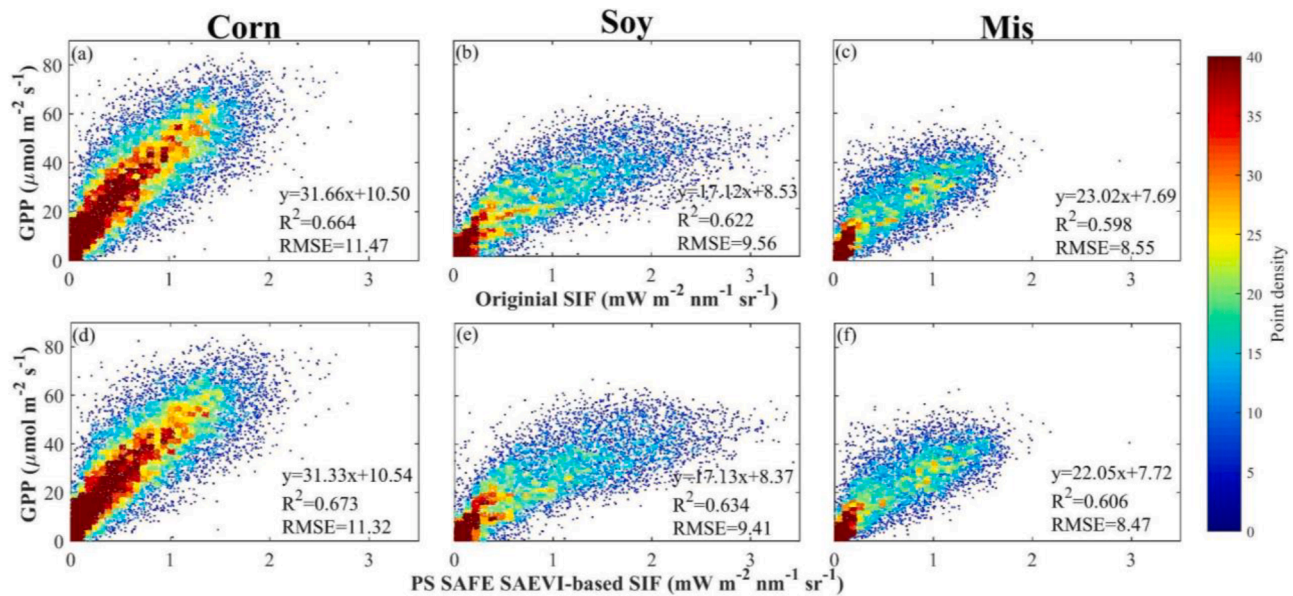


Fig. 9. The scatterplot between original SIF and GPP as well as footprint corrected SIF using PS data, SAFE EC footprint model and SAEVI, and GPP at the half-hourly timestamp. Colormap represents point density. The linear regression equation and R^2 were shown in each sub-figure.

4. Discussion

4.1. Evaluation of footprint-to-target-area representativeness in croplands

Consistent with our hypothesis, the SIF-GPP relationships were not substantially changed after upscaling the nadir SIF to flux footprint at our crop sites (Figs. 5–8). Corn and soybean are row-planting crops that result in relatively homogenous field conditions compared to natural ecosystems (Gunsolus, 1990), although in-field variations of soil and topographic properties could cause some heterogeneities (Jiang and Thelen, 2004; Vieira and Gonzalez, 2003). Miscanthus emerged annually after its establishment in 2010 (Moore et al., 2020). Some

heterogeneities were observed in the miscanthus field with high NIRv shown in the southern edges and low NIRv in the northern edges, but the SIF tower and EC tower were located in the middle of the field which well represented the average conditions of the field. Additionally, SIF tower and EC tower were close to each other within 10 m to 50 m. Considering that the major contributing area of EC flux comes from the area close to the EC tower (Kljun et al., 2015), the small distance between SIF and EC towers increased representativeness of the SIF target within the EC footprint. In this study, we used VIs calculated from high spatiotemporal satellite reflectance data to evaluate the heterogeneity within the field and upscale the nadir SIF to EC footprint considering the strong correlation between SIF and structural VIs (Doughty et al., 2021;

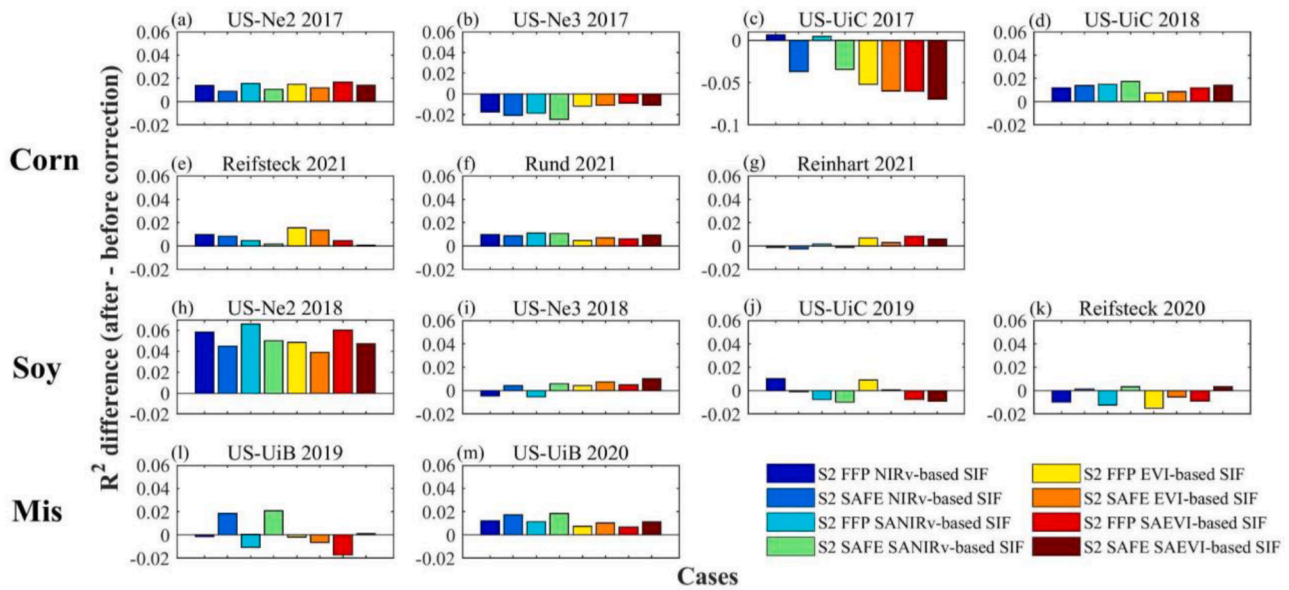


Fig. A1. The R^2 of SIF-GPP changes after the footprint correction at each individual site-year. Different colors represent 8 different scenarios using S2 data, two EC footprint models (FFP and SAFE), and four VIs (NIRv, SANIRv, EVI, and SAEVI).

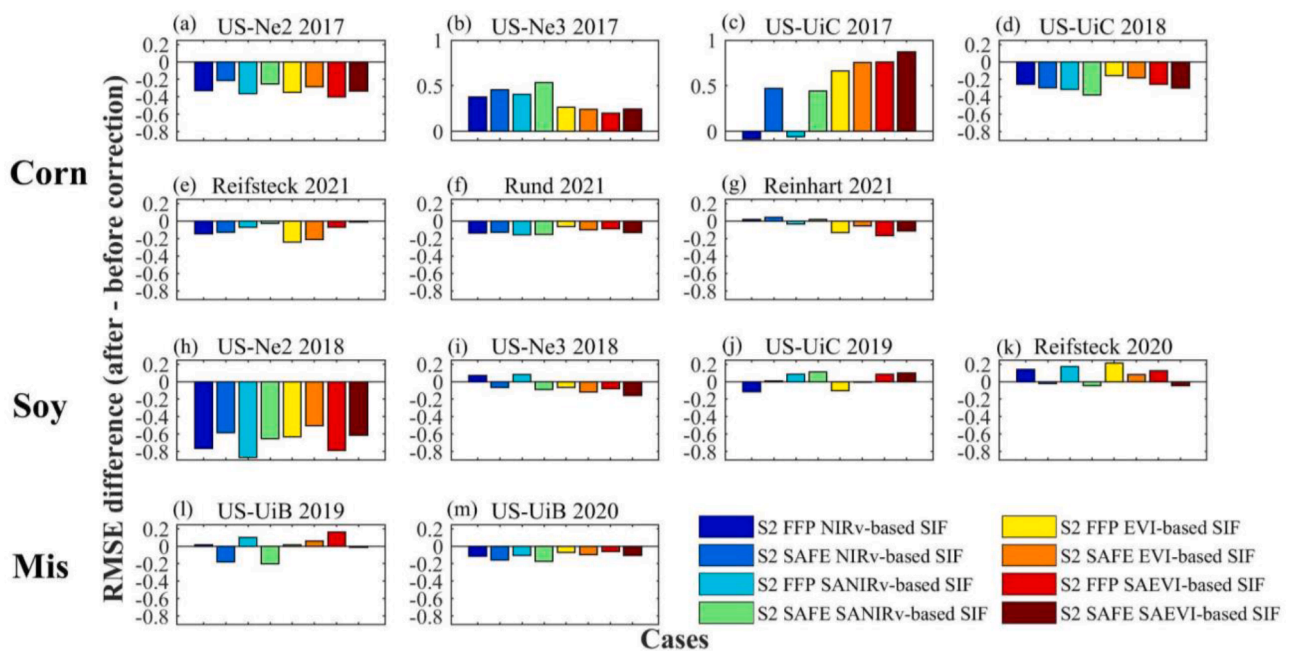


Fig. A2. The RMSE of SIF-GPP changes after the footprint correction at each individual site-year. Different colors represent 8 different scenarios using S2 data, two EC footprint models (FFP and SAFE), and four VIs (NIRv, SANIRv, EVI, and SAEVI).

Turner et al., 2020; Zeng et al., 2022b). Previous studies have used VIs or reflectance directly to downscale coarse satellite SIF to finer spatial scale SIF products (Gensheimer et al., 2022; Turner et al., 2020; Zhang et al., 2018). Upscaling SIF to a fixed footprint, $100\text{ m} \times 100\text{ m}$ centered on the flux tower, did not significantly change the SIF-GPP relationship, which further demonstrated the homogeneity of our crop site within the EC footprint (Fig. S10 – S13). Although our study only focused on croplands with relatively homogenous field conditions, the methods we proposed could be potentially applied to other ecosystems where EVI and NIRv can explain the majority variation of SIF such as deciduous broadleaf forest and grassland (Dechant et al., 2022; Doughty et al., 2021; Guo et al., 2022). For natural ecosystems, more heterogeneities within the EC footprint are observed (Chu et al., 2021), and a larger change of SIF-GPP

relationships after upscaling nadir SIF to EC footprint would be expected. We note that a recent study has shown that matching NIRv with EC footprint could improve GPP estimation when crop and wetland sites are combined (Kong et al., 2022). We conducted the same analysis at our crop sites and found the relationship between GPP and NIRvP did not substantial change among NIRv from different sampling areas including SIF tower pixel, fixed footprint of $100\text{ m} \times 100\text{ m}$ centered on the flux tower, and EC footprint. R^2 of GPP-NIRvP slightly declined when NIRv sampled from a $250\text{ m} \times 250\text{ m}$ centered on the flux tower which was larger than average EC footprint and field size at US-UiC and US-UiB sites (Fig. S14). These results further demonstrate that the spectral tower sampling area well represents the EC footprint in croplands, and indirectly support that our upscaling method can be potentially applied

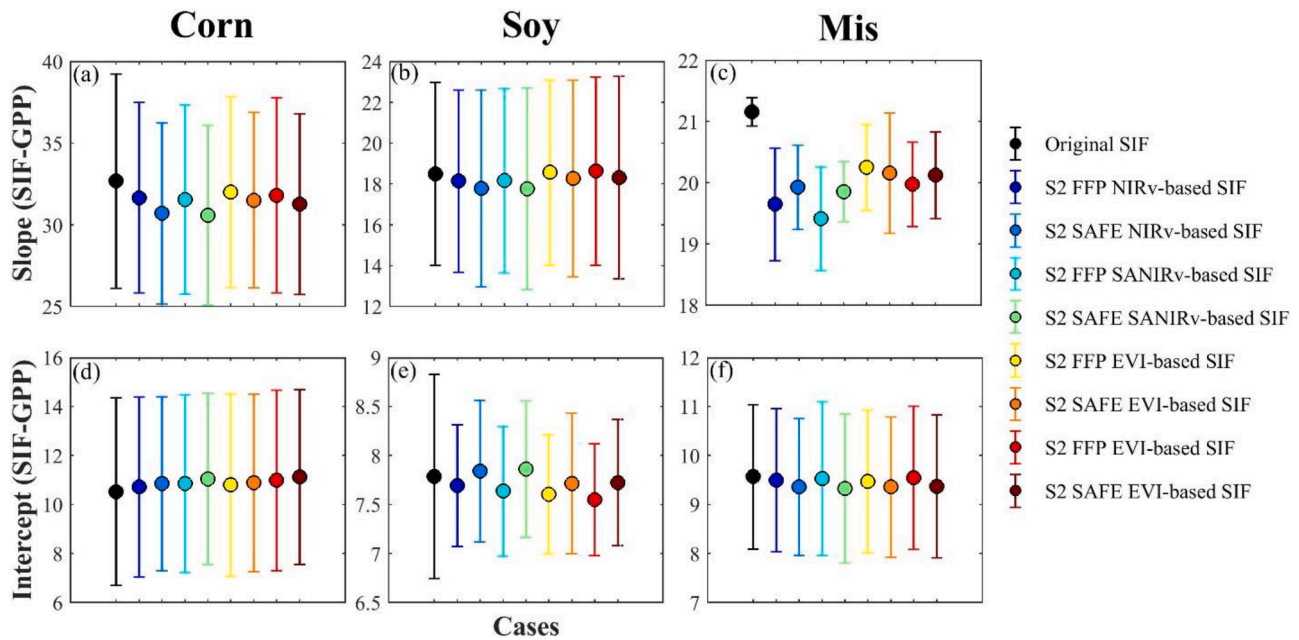


Fig. A3. The regression slope and intercept variation across different site-years within corn (a, d), soybean (b, e), and miscanthus (c, f) for the original SIF (black dots) and footprint corrected SIF (colored dots) using S2 data, two EC footprint models (FFP and SAFE) and four VIs (NIRv, SANIRv, EVI and SAEVI). Data shown are mean \pm standard deviation.

to more heterogeneous ecosystems where selected VIs can explain the majority variation of SIF and GPP.

4.2. Comparison of different VIs, EC footprint models, and satellite data

Overall, different cases calculated from different VIs, EC footprint models, and satellite data led to marginal differences in the SIF-GPP relationships when upscaling nadir SIF to EC footprint. We note that different site-years showed differences in the change of SIF-GPP relationship after SIF upscaling, e.g., the largest increase in R^2 of SIF-GPP in US-Ne2 soybean among all the cases (Fig. 5). These differences are largely caused by the representativeness of spectral tower location to EC footprint and different data availability periods at each site-year (Miao et al., 2020). Although some of previous studies have reported a slightly stronger correlation between SIF and NIRv compared to EVI at the global scale (Zeng et al., 2022b), the advantage of NIRv over EVI depends on the regions and ecosystems (Doughty et al., 2021). For example, higher temporal correlation between SIF and EVI has been shown in tropics and subtropics (Doughty et al., 2021). Crop NIRv and EVI in our study showed a similar correlation with SIF at both spatial and temporal scales (Fig. 2 & Fig. S15). Compared to original VIs, the soil adjustment process of VIs exerted a slightly larger difference in the SIF-GPP relationships. Soil-adjusted VI showed near-zero values at the early and end of the growing season (Fig. S16), which can better capture the variation of SIF at low vegetation cover (Jiang et al., 2020; Zeng et al., 2019). The ratio of EC footprint-weighted soil-adjusted VI to SIF tower pixel soil-adjusted VI showed larger deviations from 1 at the early and end of growing season compared to that of non-soil-adjusted VI (Fig. 3 & Fig. S5). This larger ratio deviation from 1 caused larger modifications of SIF from soil-adjusted VIs at the early and end of growing season, which further slightly decreased the variation of SIF across the whole growing season and marginally improved SIF-GPP relationships.

Different footprint models with varying complexity and assumptions can result in different flux contributions along with the distance from the EC tower (Arriga et al., 2017; Leclerc et al., 2014). EC footprint calculated from the SAFE model covered a larger area compared to the FFP model, which resulted in a slightly higher R^2 increase of SIF-GPP after SIF footprint upscaling at some site-years (e.g., US-UiC 2017 and US-Ne2

2018). The different uses of measurement height contributed partly to the differences between these two models. For the SAFE model, the recorded EC instrument height was used (Chen et al., 2009), while for FFP, the difference between instrument height and displacement height was used (Kljun et al., 2015). Using the z_m of FFP in the SAFE model resulted in smaller EC footprint coverage compared to the raw z_m (Fig. S17). Additionally, the SAFE model used EC-measured NEE to weight the pure footprint which was only determined by atmospheric stability, wind speed and wind direction, while the FFP model only used atmospheric information, which could lead to the footprint differences between SAFE and FFP. More direct validation is needed to verify the performance of different EC footprint models.

Regarding the different satellite reflectance data, the higher temporal resolution of PS which resulted in less uncertainty for daily interpolation, and higher spatial resolution of PS (i.e., 3 m) which better represented the SIF tower targeting area caused slightly better performance of PS compared to S2 in upscaling nadir SIF to EC footprint when all cases were considered (Fig. 8 & A4). Some studies have demonstrated the improved performance of PS over S2 to detect fine spatial and temporal scale phenology and land cover classification (Cheng et al., 2020; Gašparović et al., 2018; Moon et al., 2021). Our study focused on cropland with relatively homogeneous field conditions, therefore the difference caused by different VIs, EC footprint models, and satellite data were marginal. Large differences among different cases would be expected in ecosystems with more heterogeneities. Future studies could apply the analyses we conducted to larger far-red SIF and GPP data collections such as ChinaSpec (Y. Zhang et al., 2021) which could provide insights across ecosystems.

4.3. Uncertainties in this study

We acknowledge that there are four main uncertainties, including the assumption of similar $\Phi_{F, canopy}$ for the homogeneous crop canopy, the negligence of PAR variation within the field, the interpolation of the satellite reflectance data, and the variations of the SIF-VI relationships. $\Phi_{F, canopy}$ depends on the absorbed energy partition among photochemistry, fluorescence and non-photochemical quenching (Frankenberg and Berry, 2018). It changes with environmental

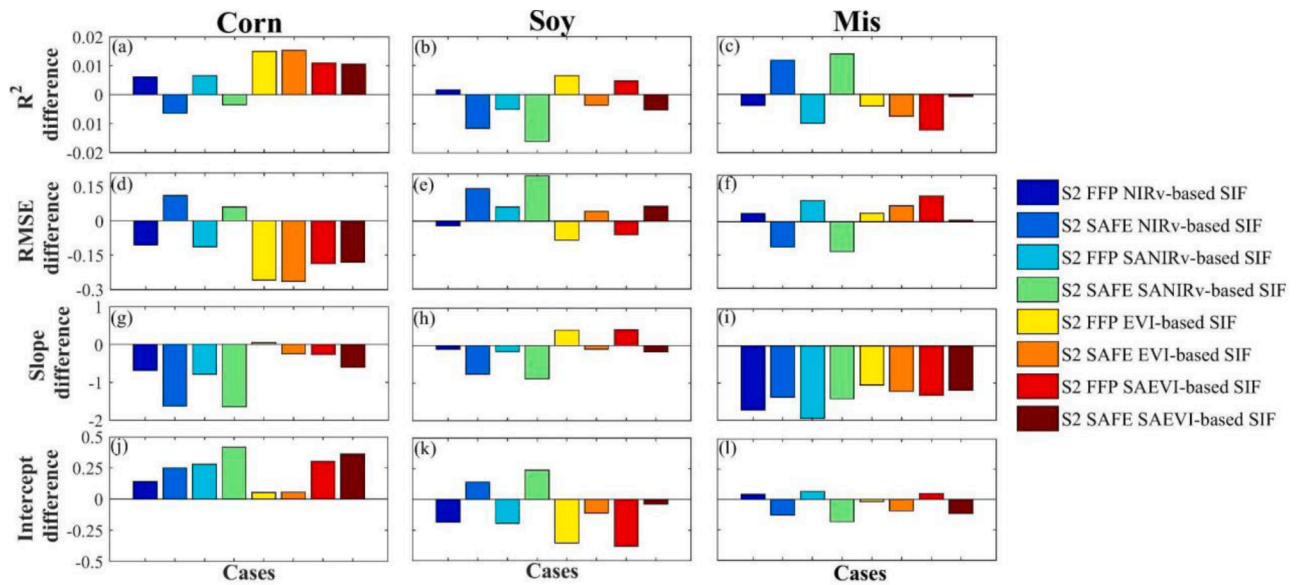


Fig. A4. The overall SIF-GPP relationship change (R^2 , RMSE, regression slope, and intercept) after the footprint correction for each species when data from all site-years for the same species are combined. A total of 8 cases using S2 data, two EC footprint models (FFP and SAFE), and four VIs (NIRv, SANIRv, EVI, and SAEVI) were considered.

conditions such as stresses (Porcar-Castell et al., 2021). Relatively stable $\Phi_{F, canopy}$ has been reported at the seasonal scale in croplands (Dechant et al., 2020). Spatial variation of $\Phi_{F, canopy}$ has been shown over the water limitation and heat stress crop sites where SIF and the product of NIRv and near-infrared irradiance (NIRvR) also showed large spatial variations (Zeng et al., 2022a). SIF and NIRvP were similar over the EC footprint in our crop sites. We expect that $\Phi_{F, canopy}$ is similar over the EC footprint, which is indirectly supported by the strong correlation between SIF and selected $VI \times PAR$ (Fig. 2). The variation of PAR between the SIF tower located pixel and the EC footprint was not considered. This assumption is valid within a radius of 500 m in the field during sunny conditions (Jiang et al., 2020), although it might bring some uncertainties under scattered cloudy conditions. We are aware that the interpolation algorithm to get daily reflectance data would bring some uncertainties, but the same algorithm was applied to all the pixels in each field, and we used the ratio of EC footprint weighted VI and SIF pixel VI to upscale the original nadir SIF. This ratio calculation is expected to cancel out the uncertainties related to the interpolation algorithm. Regarding the variations of SIF-VI relationships, recent cross-scale studies have found that the product of NIRv and PAR (NIRvP) can explain around 80% of SIF variations when combining spatial and temporal scales (Dechant et al., 2022; Kimm et al., 2021). Our portable campaign also confirmed that the product of EVI and PAR as well as NIRvP could explain 85% to 90% variations in SIF signal in corn and soybean (Fig. 2), which demonstrated that our method captured the majority of SIF difference between EC footprint and SIF tower area even without considering the variation of SIF-VI relationships. Therefore, we justify that these uncertainties do not affect our general conclusions.

4.4. Implications to the SIF-GPP research in croplands

SIF-GPP relationships are affected by canopy structure (Dechant et al., 2020; Miao et al., 2018), leaf physiology (Wu et al., 2022a; Yang et al., 2021), instrumentation and data process uncertainties (Zhang et al., 2019). Matching in-situ SIF collected by the same spectral system and processed with the same protocol with EC footprint did not change the SIF-GPP relationships for individual site-years in our study, indicating that canopy structure and leaf physiology are the major factors causing different SIF-GPP relationships among corn, soybean, and

miscanthus (Fig. 8). The strongest SIF-GPP relationship shown in corn was due to the fact that both SIF and GPP co-varied with APAR (Yang et al., 2021), while for soybean, GPP did not co-vary with APAR at the seasonal scale (Wu et al., 2022b), and for miscanthus, SIF did not co-vary with APAR at the diurnal scale (Wu et al., 2022a). Those patterns caused the weaker correlations between SIF and GPP in soybean and miscanthus compared to corn (Fig. 8). This phenomenon of species-dependent SIF-GPP relationships challenges the use of a single SIF-GPP relationship within one plant functional type (PFT) adopted in previous studies (Guanter et al., 2014; Zhang et al., 2020). Combining other canopy structure and leaf physiology variables with SIF is expected to improve GPP estimation better. Previous studies have found that combining SIF with photochemical reflectance index (PRI) which can account for part of NPQ information can improve GPP estimations across various species (Schickling et al., 2016; Wang et al., 2020). More observations that cover different species with both fluorescence and photosynthesis processes included would be helpful to understand the SIF-GPP relationships better and build one generic SIF-GPP relationship across various species.

5. Conclusion

We upscaled 13 site-years of nadir SIF to EC footprint using VIs from high spatiotemporal satellite reflectance data and investigated the change of SIF-GPP relationships for three crop species: corn, soybean, and miscanthus. We found that the field conditions were overall homogenous across all the site-years, and SIF-GPP relationships did not considerably change after the SIF target area upscaling. NIRv and EVI showed similar performance in nadir SIF upscaling. EC footprint calculated from the SAFE model which covered a larger area compared to the FFP model showed a slightly larger increase of R^2 of SIF-GPP after the upscaling at some site-years. Overall, using VIs calculated from PS showed a larger increase of R^2 compared to S2 due to the higher spatiotemporal resolutions of PS data. The variations of regression slopes and intercepts across different site-years within each species were overall similar between original nadir SIF and upscaled EC footprint SIF. Our results demonstrated that the spatial mismatch between ground nadir SIF and GPP was a marginal issue for investigating the SIF-GPP relationship in croplands. The methods we proposed in this study could be potentially applied to other ecosystems with more

heterogeneities.

Declaration of Competing Interest

The authors declare that they have no known competing financial interests or personal relationships that could have appeared to influence the work reported in this paper.

Data availability

Data will be made available on request.

Acknowledgements

GW, KG, and HK acknowledged the support from NASA Carbon Monitoring System program managed by the NASA Terrestrial Ecology Program. GW, KG, CJ, CB and CE acknowledge the support from DOE Center for Advanced Bioenergy and Bioproducts Innovation (U.S. Department of Energy, Office of Science, Office of Biological and Environmental Research under Award Number DE-SC0018420). Any opinions, findings, and conclusions or recommendations expressed in this publication are those of the author (s) and do not necessarily reflect the views of the U.S. Department of Energy. KG, CJ, CB and XS acknowledge the support from the Advanced Research Projects Agency–Energy (ARPA-E), US Department of Energy, under award number DE-AR0001382. GW and KG acknowledged the support from NASA Future Investigators in NASA Earth and Space Science and Technology (FINESST) Program. We thank Dr. Andy Suyker for the Nebraska field sites management and support, and Dr. Carl Bernacchi for the Illinois field sites support. We thank M. Pilar Cendrero-Mateo for sharing code for iFLD SIF retrieval.

Supplementary materials

Supplementary material associated with this article can be found, in the online version, at [doi:10.1016/j.agrformet.2023.109532](https://doi.org/10.1016/j.agrformet.2023.109532).

Appendix

The change of SIF-GPP relationship after upscaling ground nadir SIF to EC footprint based on S2 VIs.

References

- Alonso, L., Gómez-Chova, L., Vila-Francés, J., Amorós-López, J., Guanter, L., Calpe, J., Moreno, J., Gomez-Chova, L., Vila-Frances, J., Amoros-Lopez, J., Guanter, L., Calpe, J., Moreno, J., Frances, Alonso Luis Vila, Lopez, Joan Amoros, Guanter, Julia, Calpe, Luis, Moreno, Javier, José, L.C., Alonso, L., Gomez-Chova, L., Vila-Frances, J., Amorós-López, J., Guanter, L., Calpe, J., Moreno, J., Gómez-Chova, L., Vila-Francés, J., Amorós-López, J., Guanter, L., Calpe, J., Moreno, J., 2008. Improved Fraunhofer Line Discrimination Method for Vegetation Fluorescence Quantification. *IEEE Geosci. Remote Sens. Lett.* 5, 620–624. <https://doi.org/10.1109/LGRS.2008.2001180>.
- Arriga, N., Rannik, Ü., Aubinet, M., Carrara, A., Vesala, T., Papale, D., 2017. Experimental validation of footprint models for eddy covariance CO₂ flux measurements above grassland by means of natural and artificial tracers. *Agric. For. Meteorol.* 242, 75–84. <https://doi.org/10.1016/j.agrformet.2017.04.006>.
- Badgley, G., Field, C.B., Berry, J.A., 2017. Canopy near-infrared reflectance and terrestrial photosynthesis. *Sci. Adv.* 3, 1602244 <https://doi.org/10.1126/sciadv.1602244>.
- Baldocchi, D., Falge, E., Gu, L., Olson, R., Hollinger, D., Running, S., Anthoni, P., Bernhofer, C., Davis, K., Evans, R., Fuentes, J., Goldstein, A., Katul, G., Law, B., Lee, X., Malhi, Y., Meyers, T., Munger, W., Oechel, W., Paw, U.K.T., Pilegaard, K., Schmid, H.P., Valentini, R., Verma, S., Vesala, T., Wilson, K., Wofsy, S., Allen, F., Katul, G., Law, J.B., Lee, X., Malhi, Y., Meyers, T., Munger, W., Oechel, W., Paw, K.T. U., H. K.P., Valentini, P.S.R., Verma, S., Vesala, T., Wilson, K., Wofsy, S., 2001. FLUXNET: A New Tool to Study the Temporal and Spatial Variability of Ecosystem-Scale Carbon Dioxide, Water Vapor, and Energy Flux Densities. *Bull. Am. Meteorol. Soc.* 82, 2415–2434. [https://doi.org/10.1175/1520-0477\(2001\)082<2415:FANTTS>2.3.CO;2](https://doi.org/10.1175/1520-0477(2001)082<2415:FANTTS>2.3.CO;2).
- Baldocchi, D.D., 2003. Assessing the eddy covariance technique for evaluating carbon dioxide exchange rates of ecosystems: Past, present and future. *Glob. Chang. Biol.* 9, 479–492. <https://doi.org/10.1046/J.1365-2486.2003.00629.X>.
- Balidoy Baloloy, A., Conferido Blanco, A., Gumbao Candido, C., Jay Labadisos Argamosa, R., Bart Lovern Caboboy Dumalag, J., Lee Carandang Dimapilis, Lady, Camero Paringit, E., 2018. Estimation of mangrove forest aboveground biomass using multispectral bands, vegetation indices and biophysical variables derived from optical satellite imageries: rapideye, planetscope and sentinel-2. In: *ISPRS Annals of the Photogrammetry, Remote Sensing and Spatial Information Sciences*, pp. 29–36. <https://doi.org/10.5194/isprs-annals-IV-3-29-2018>.
- Cendrero-Mateo, M.P., Wieneke, S., Damm, A., Alonso, L., Pinto, F., Moreno, J., Guanter, L., Celesti, M., Rossini, M., Sabater, N., Cogliati, S., Julitta, T., Rascher, U., Goulas, Y., Aasen, H., Pacheco-Labrador, J., Arthur, A.Mac, 2019. Sun-induced chlorophyll fluorescence III: Benchmarking retrieval methods and sensor characteristics for proximal sensing. *Remote Sens.* 11, 962. <https://doi.org/10.3390/rs11080921>.
- Chen, B., Black, T.A., Coops, N.C., Hilker, T., Trofymow, J.A., Morgenstern, K., 2009. Assessing tower flux footprint climatology and scaling between remotely sensed and eddy covariance measurements. *Boundary-Layer Meteorol.* 130, 137–167. <https://doi.org/10.1007/s10546-008-9339-1>.
- Cheng, Y., Vrieling, A., Fava, F., Meroni, M., Marshall, M., Gachoki, S., 2020. Phenology of short vegetation cycles in a Kenyan rangeland from PlanetScope and Sentinel-2. *Remote Sens. Environ.* 248 <https://doi.org/10.1016/j.rse.2020.112004>.
- Chu, H., Luo, X., Ouyang, Z., Chan, W.S., Dengel, S., Biraud, S.C., Torn, M.S., Metzger, S., Kumar, J., Arain, M.A., Arkebauer, T.J., Baldocchi, D., Bernacchi, C., Billesbach, D., Black, T.A., Blanken, P.D., Bohrer, G., Bracho, R., Brown, S., Brunsell, N.A., Chen, J., Chen, X., Clark, K., Desai, A.R., Duman, T., Durden, D., Fares, S., Forbrich, I., Gamon, J.A., Gough, C.M., Griffiths, T., Helbig, M., Hollinger, D., Humphreys, E., Ikawa, H., Iwata, H., Ju, Y., Knowles, J.F., Knox, S.H., Kobayashi, H., Kolb, T., Law, B., Lee, X., Litvak, M., Liu, H., Munger, J.W., Noormets, A., Novick, K., Oberbauer, S.F., Oechel, W., Oikawa, P., Papuga, S.A., Pendall, E., Prajapati, P., Prueger, J., Quinton, W.L., Richardson, A.D., Russell, E.S., Scott, R.L., Starr, G., Staebler, R., Stoy, P.C., Stuart-Haëntjens, E., Sonnentag, O., Sullivan, R.C., Suyker, A., Ueyama, M., Vargas, R., Wood, J.D., Zona, D., 2021. Representativeness of Eddy-Covariance flux footprints for areas surrounding AmeriFlux sites. *Agric. For. Meteorol.* 301–302, 108350 <https://doi.org/10.1016/j.agrformet.2021.108350>.
- Csillik, O., Kumar, P., Mascaro, J., O'Shea, T., Asner, G.P., 2019. Monitoring tropical forest carbon stocks and emissions using Planet satellite data. *Sci. Rep.* 9, 1–12. <https://doi.org/10.1038/s41598-019-54386-6>, 2019 91.
- Dechant, B., Ryu, Y., Badgley, G., Köhler, P., Rascher, U., Migliavacca, M., Zhang, Y., Tagliabue, G., Guan, K., Rossini, M., Goulas, Y., Zeng, Y., Frankenberg, C., Berry, J.A., 2022. NIRVP: A robust structural proxy for sun-induced chlorophyll fluorescence and photosynthesis across scales. *Remote Sens. Environ.* 268 <https://doi.org/10.1016/j.rse.2021.112763>.
- Dechant, B., Ryu, Y., Badgley, G., Zeng, Y., Berry, J.A., Zhang, Y., Goulas, Y., Li, Z., Zhang, Q., Kang, M., Li, J., Moya, I., 2020. Canopy structure explains the relationship between photosynthesis and sun-induced chlorophyll fluorescence in crops. *Remote Sens. Environ.* 241 <https://doi.org/10.1016/j.rse.2020.111733>.
- Doughty, R., Xiao, X., Köhler, P., Frankenberg, C., Qin, Y., Wu, X., Ma, S., Moore, B., 2021. Global-Scale Consistency of Spaceborne Vegetation Indices, Chlorophyll Fluorescence, and Photosynthesis. *J. Geophys. Res. Biogeosciences* 126. <https://doi.org/10.1029/2020JG006136>.
- Du, S., Liu, L., Liu, X., Guo, J., Hu, J., Wang, S., Zhang, Y., 2019. SIFSpec: Measuring Solar-Induced Chlorophyll Fluorescence Observations for Remote Sensing of Photosynthesis. *Sensors* 19, 3009. <https://doi.org/10.3390/S19133009>, 2019, Vol. 19, Page 3009.
- Duveiller, G., Filippini, F., Walther, S., Köhler, P., Frankenberg, C., Guanter, L., Cescatti, A., 2020. A spatially downscaled sun-induced fluorescence global product for enhanced monitoring of vegetation productivity. *Earth Syst. Sci. Data* 12, 1101–1116. <https://doi.org/10.5194/ESSD-12-1101-2020>.
- Foken, T., Leclerc, M.Y., 2004. Methods and limitations in validation of footprint models. *Agric. For. Meteorol.* 127, 223–234. <https://doi.org/10.1016/J.AGRFORMET.2004.07.015>.
- Frankenberg, C., Berry, J., 2018. Solar Induced Chlorophyll Fluorescence: Origins, Relation to Photosynthesis and Retrieval, Comprehensive Remote Sensing. Elsevier. <https://doi.org/10.1016/B978-0-12-409548-9.10632-3>.
- Frankenberg, C., Fisher, J.B., Worden, J., Badgley, G., Saatchi, S.S., Lee, J.E., Toon, G.C., Butz, A., Jung, M., Kuze, A., Yokota, T., 2011. New global observations of the terrestrial carbon cycle from GOSAT: Patterns of plant fluorescence with gross primary productivity. *Geophys. Res. Lett.* 38, 1–22. <https://doi.org/10.1029/2011GL048738>.
- Gasparović, M., Medak, D., Pilaš, I., Jurjević, L., Balenović, I., 2018. Fusion of sentinel-2 and planetscope imagery for vegetation detection and monitoring. In: *International Archives of the Photogrammetry, Remote Sensing and Spatial Information Sciences - ISPRS Archives*, pp. 155–160. <https://doi.org/10.5194/isprs-archives-XLII-1-155-2018>.
- Gensheimer, J., Turner, A.J., Köhler, P., Frankenberg, C., Chen, J., Gensheimer johannesgensheimer, J., Chen jiachen, J., 2022. A convolutional neural network for spatial downscaling of satellite-based solar-induced chlorophyll fluorescence (SIFnet). *Biogeosciences* 19, 1777–1793. <https://doi.org/10.5194/bg-19-1777-2022>.
- Grossmann, K., Hurlock, S.C., Seibt, U., Stutz, J., Frankenberg, C., Magney, T.S., Hurlock, S.C., Seibt, U., Stutz, J., 2018. PhotoSpec: A new instrument to measure spatially distributed red and far-red Solar-Induced Chlorophyll Fluorescence. *Remote Sens. Environ.* 216, 311–327. <https://doi.org/10.1016/j.rse.2018.07.002>.

- Gu, L., Wood, J.D., Chang, C.Y.Y.-Y., Sun, Y., Riggs, J.S., 2019. Advancing Terrestrial Ecosystem Science With a Novel Automated Measurement System for Sun-Induced Chlorophyll Fluorescence for Integration With Eddy Covariance Flux Networks. *J. Geophys. Res. Biogeosciences* 124, 127–146. <https://doi.org/10.1029/2018JG004742>.
- Guanter, L., Zhang, Y., Jung, M., Joiner, J., Voigt, M., Berry, J.A., Frankenberg, C., Huete, A.R., Zarco-Tejada, P., Lee, J.E.J.-E., Moran, M.S., Ponce-Campos, G., Beer, C., Camps-Valls, G., Buchmann, N., Gianelle, D., Klumpp, K., Cescatti, A., Baker, J.M., Griffis, T.J., 2014. Global and time-resolved monitoring of crop photosynthesis with chlorophyll fluorescence. *Proc. Natl. Acad. Sci.* 111, E1327–E1333. <https://doi.org/10.1073/pnas.1320008111>.
- Gunsolus, J.L., 1990. Mechanical and cultural weed control in corn and soybeans. *Am. J. Altern. Agric.* 5, 114–119. <https://doi.org/10.1017/S0889189300003416>.
- Guo, M., Li, Jing, Li, Jianuo, Zhong, C., Zhou, F., 2022. Solar-Induced Chlorophyll Fluorescence Trends and Mechanisms in Different Ecosystems in Northeastern China. *Remote Sens.* 14, 1–17. <https://doi.org/10.3390/rs14061329>.
- Heaton, E.A., Dohleman, F.G., Miguez, A.F., Juvik, J.A., Lozovaya, V., Widholm, J., Zabolina, O.A., McIsaac, G.F., David, M.B., Voigt, T.B., Boersma, N.N., Long, S.P., 2010. Miscanthus. A Promising Biomass Crop, in: *Advances in Botanical Research*. pp. 75–137. <https://doi.org/10.1016/B978-0-12-381518-7.00003-0>.
- Houborg, R., McCabe, M.F., 2016. High-Resolution NDVI from Planet's Constellation of Earth Observing Nano-Satellites: A New Data Source for Precision Agriculture. *Remote Sens.* 8, 768. <https://doi.org/10.3390/RS8090768>, 2016, Vol. 8, Page 768.
- Immitzer, M., Vuolo, F., Atzberger, C., Sarathi Roy, P., Thenkabail, P.S., 2016. First Experience with Sentinel-2 Data for Crop and Tree Species Classifications in Central Europe. *Remote Sens.* 8, 166. <https://doi.org/10.3390/RS8030166>, 2016, Vol. 8, Page 166.
- Jiang, C., Guan, K., Wu, G., Peng, B., Wang, S., 2020. A daily, 250 m, and real-time gross primary productivity product (2000 – present) covering the Contiguous United States. *Earth Syst. Sci. Data* 1786.
- Jiang, P., Thelen, K.D., 2004. Effect of Soil and Topographic Properties on Crop Yield in a North-Central Corn-Soybean Cropping System. *Agron. J.* 96, 252–258. <https://doi.org/10.2134/agronj2004.0252>.
- Kamenova, I., Dimitrov, P., 2021. Evaluation of Sentinel-2 vegetation indices for prediction of LAI, fAPAR and fCover of winter wheat in Bulgaria. *Eur. J. Remote Sens.* 54, 89–108. <https://doi.org/10.1080/22797254.2020.1839359/FORMAT/EPUB>.
- Kimm, H., Guan, K., Jiang, C., Miao, G., Wu, G., Suyker, A.E., Ainsworth, E.A., Bernacchi, C.J., Montes, C.M., Berry, J.A., Yang, X., Frankenberg, C., Chen, M., Köhler, P., 2021. A physiological signal derived from sun-induced chlorophyll fluorescence quantifies crop physiological response to environmental stresses in the U.S. Corn Belt. *Environ. Res. Lett.* 16, 124051 <https://doi.org/10.1088/1748-9326/ac3b16>.
- Kimm, H., Guan, K., Jiang, C., Peng, B., Gentry, L.F., Wilkin, S.C., Wang, S., Cai, Y., Bernacchi, C.J., Peng, J., Luo, Y., 2020. Deriving high-spatiotemporal-resolution leaf area index for agroecosystems in the U.S. Corn Belt using Planet Labs CubeSat and STAIR fusion data. *Remote Sens. Environ.* 239, 111615 <https://doi.org/10.1016/J.RSE.2019.111615>.
- Kljun, N., Calanca, P., Rotach, M.W., Schmid, H.P., 2015. A simple two-dimensional parameterisation for Flux Footprint Prediction (FFP). *Geosci. Model Dev.* 8, 3695–3713. <https://doi.org/10.5194/gmd-8-3695-2015>.
- Kong, J., Ryu, Y., Liu, J., Dechant, B., Rey-Sanchez, C., Shortt, R., Szutu, D., Verfaillie, J., Houborg, R., Baldocchi, D.D., 2022. Matching high resolution satellite data and flux tower footprints improves their agreement in photosynthesis estimates. *Agric. For. Meteorol.* 316 <https://doi.org/10.1016/J.AGRFORMET.2022.108878>.
- Kormann, R., Meixner, F.X., 2001. An Analytical Footprint Model For Non-Neutral Stratification. *Boundary-Layer Meteorol* 99(2), 207–224. <https://doi.org/10.1023/A:1018991015119>, 2001.
- Kumar, J., Hoffman, F.M., Hargrove, W.W., Collier, N., 2016. Understanding the representativeness of FLUXNET for upscaling carbon flux from eddy covariance measurements. *Earth Syst. Sci. Data Discuss.* 1–25. <https://doi.org/10.5194/ESSD-2016-36>.
- Leclercq, M.Y., Foken, T., Savage, M.J., Göckede, M., 2014. Footprints in micrometeorology and ecology. *Footprints Micrometeorol. Ecol.* <https://doi.org/10.1007/978-3-642-54545-0>.
- Li, X., Xiao, J., 2022. TROPOMI observations allow for robust exploration of the relationship between solar-induced chlorophyll fluorescence and terrestrial gross primary production. *Remote Sens. Environ.* 268 <https://doi.org/10.1016/j.rse.2021.112748>.
- Li, Z., Zhang, Q., Li, J., Yang, X., Wu, Y., Zhang, Z., Wang, S., Wang, H., Zhang, Y., 2020. Solar-induced chlorophyll fluorescence and its link to canopy photosynthesis in maize from continuous ground measurements. *Remote Sens. Environ.* 236 <https://doi.org/10.1016/j.rse.2019.111420>.
- Liu, X., Liu, L., Hu, J., Du, S., 2017. Modeling the footprint and equivalent radiance transfer path length for tower-based hemispherical observations of chlorophyll fluorescence. *Sensors (Switzerland)* 17, 1–15. <https://doi.org/10.3390/s17051131>.
- Magney, T.S., Barnes, M.L., Yang, X., 2020. On the Covariation of Chlorophyll Fluorescence and Photosynthesis Across Scales. *Geophys. Res. Lett.* 47, 1–7. <https://doi.org/10.1029/2020GL091098>.
- Mashonganyika, F., Mugiyo, H., Svatwa, E., Kutuywayo, D., 2021. Mapping of Winter Wheat Using Sentinel-2 NDVI Data. A Case of Mashonaland Central Province in Zimbabwe. *Front. Clim.* 3, 137. <https://doi.org/10.3389/FCLIM.2021.715837/BIBTEX>.
- Maurer, K.D., Bohrer, G., Kenny, W.T., Ivanov, V.Y., 2015. Large-eddy simulations of surface roughness parameter sensitivity to canopy-structure characteristics. *Biogeosciences* 12, 2533–2548. <https://doi.org/10.5194/bg-12-2533-2015>.
- Meroni, M., Rossini, M., Guanter, L., Alonso, L., Rascher, U., Colombo, R., Moreno, J., 2009. Remote sensing of solar-induced chlorophyll fluorescence : Review of methods and applications 113, 2037–2051. [10.1016/j.rse.2009.05.003](https://doi.org/10.1016/j.rse.2009.05.003).
- Miao, G., Guan, K., Suyker, A.E., Yang, X., Arkebauer, T.J., Walter-Shea, E.A., Kimm, H., Hmimina, G.Y., Gamon, J.A., Franz, T.E., Frankenberg, C., Berry, J.A., Wu, G., 2020. Varying Contributions of Drivers to the Relationship Between Canopy Photosynthesis and Far-Red Sun-Induced Fluorescence for Two Maize Sites at Different Temporal Scales. *J. Geophys. Res. Biogeosciences* 125, 1–17. <https://doi.org/10.1029/2019JG005051>.
- Miao, G., Guan, K., Yang, X., Bernacchi, C.J., Berry, J.A., DeLucia, E.H., Wu, J., Moore, C.E., Meacham, K., Cai, Y., Peng, B., Kimm, H., Masters, M.D., 2018. Sun-Induced Chlorophyll Fluorescence, Photosynthesis, and Light Use Efficiency of a Soybean Field from Seasonally Continuous Measurements. *J. Geophys. Res. Biogeosciences* 123, 610–623. <https://doi.org/10.1002/2017JG004180>.
- Moon, M., Richardson, A.D., Friedl, M.A., 2021. Multiscale assessment of land surface phenology from harmonized Landsat 8 and Sentinel-2, PlanetScope, and PhenoCam imagery. *Remote Sens. Environ.* 266, 112716 <https://doi.org/10.1016/J.RSE.2021.112716>.
- Moore, C.E., von Haden, A.C., Burnham, M.B., Kantola, I.B., Gibson, C.D., Blakely, B.J., Dracup, E.C., Masters, M.D., Yang, W.H., DeLucia, E.H., Bernacchi, C.J., 2020. Ecosystem-scale biogeochemical fluxes from three bioenergy crop candidates: How energy sorghum compares to maize and miscanthus. *GCB Bioenergy* 13, 445–458. <https://doi.org/10.1111/gcb.12788>.
- Mudreri, B.T., Dube, T., Adel-Rahman, E.M., Niassy, S., Kimathi, E., Khan, Z., Landmann, T., 2019. A comparative analysis of PlanetScope and Sentinel-2 space-borne sensors in mapping Striga weed using Guided Regularised Random Forest classification ensemble. [10.5194/isprs-archives-XLII-2-W13-701-2019](https://doi.org/10.5194/isprs-archives-XLII-2-W13-701-2019).
- Pastorello, G., Trotta, C., Canfora, E., Chu, H., Christianson, D., Cheah, Y.W., Poindexter, C., Chen, J., Elbasshandy, A., Humphrey, M., Isaac, P., Polidori, D., Ribeca, A., van Ingen, C., Zhang, L., Amiro, B., Ammann, C., Arain, M.A., Ardö, J., Arkebauer, T., Arndt, S.K., Arriga, N., Aubinet, M., Aurela, M., Baldocchi, D., Barr, A., Beamesderfer, E., Marchesini, L.B., Bergeron, O., Beringer, J., Bernhofer, C., Berveiller, D., Billesbach, D., Black, T.A., Blanken, P.D., Bohrer, G., Boike, J., Bolstad, P. V., Bonal, D., Bonnefond, J.M., Bowling, D.R., Bracho, R., Brodeur, J., Brümmer, C., Buchmann, N., Burban, B., Burns, S.P., Buysse, P., Cale, P., Cavagna, M., Cellier, P., Chen, S., Chini, I., Christensen, T.R., Cleverly, J., Collati, A., Consalvo, C., Cook, B.D., Cook, D., Coursolle, C., Cremonese, E., Curtis, P.S., D'Andrea, E., da Rocha, H., Dai, X., Davis, K.J., De Cinti, B., de Grandcourt, A., De Ligne, A., De Oliveira, R.C., Delpierre, N., Desai, A.R., Di Bella, C.M., di Tommasi, P., Dolman, H., Domingo, F., Dong, G., Dore, S., Duce, P., Dufrene, E., Dunn, A., Dušek, J., Eamus, D., Eichmann, U., Elkhidir, H.A.M., Eugster, W., Ewenz, C.M., Ewers, B., Famulari, D., Fares, S., Feigenwinter, I., Feitz, A., Fensholt, R., Filippa, G., Fischer, M., Frank, J., Galvagno, M., Gharun, M., Gianelle, D., Gielen, B., Glioli, B., Gitelson, A., Godec, I., Goeckede, M., Goldstein, A.H., Gough, C.M., Goulden, M.L., Graf, A., Griebel, A., Gruening, C., Grünwald, T., Hammerle, A., Han, S., Han, X., Hansen, B. U., Hanson, C., Hatakka, J., He, Y., Hehn, M., Heinesch, B., Hinko-Najera, N., Hörtnagl, L., Hutley, L., Ibrom, A., Ikawa, H., Jackowicz-Korczynski, M., Janouš, D., Jans, W., Jassal, R., Jiang, S., Kato, T., Khomik, M., Klatt, J., Knohl, A., Knox, S., Kobayashi, H., Koerber, G., Kolbe, O., Kosugi, Y., Kotani, A., Kowalski, A., Kruijt, B., Kurbatova, J., Kutsch, W.L., Kwon, H., Launiainen, S., Laurila, T., Law, B., Leuning, R., Li, Yingnian, Liddell, M., Limousin, J.M., Lion, M., Liska, A.J., Lohila, A., López-Ballesteros, A., López-Blanco, E., Loubet, B., Loustau, D., Lucas-Moffat, A., Lüers, J., Ma, S., Macfarlane, C., Magliulo, V., Maier, R., Mammarella, I., Manca, G., Marcolla, B., Margolis, H.A., Marras, S., Massman, W., Mastepanov, M., Matamala, R., Matthes, J.H., Mazzenga, F., McCaughey, H., McHugh, I., McMillan, A.M.S., Merbold, L., Meyer, W., Meyers, T., Miller, S.D., Minerbi, S., Moderow, U., Monson, R.K., Montagnani, L., Moore, C.E., Moors, E., Moreaux, V., Moureaux, C., Munger, J.W., Nakai, T., Neirynck, J., Nesic, Z., Nicolini, G., Noormets, A., Northwood, M., Nössetto, M., Nouvellon, Y., Novick, K., Oechel, W., Olesen, J.E., Ourcival, J.M., Papuga, S.A., Parmentier, F.J., Paul-Limoges, E., Pavelka, M., Peichl, M., Pendall, E., Phillips, R.P., Pilegaard, K., Pirk, N., Posse, G., Powell, T., Prasse, H., Prober, S.M., Rambal, S., Rannik, Ü., Raz-Yaseef, N., Reed, D., de Dios, V.R., Restrepo-Coupe, N., Reverter, B. R., Roland, M., Sabbatini, S., Sachs, T., Saleska, S.R., Sánchez-Cañete, E.P., Sanchez-Mejia, Z.M., Schmid, H.P., Schmidt, M., Schneider, K., Schrader, F., Schroder, I., Scott, R.L., Sedláček, P., Serrano-Ortiz, P., Shao, C., Shi, P., Shironya, I., Siebicke, L., Šigut, L., Silberstein, R., Sirca, C., Spano, D., Steinbrecher, R., Stevens, R.M., Sturtevant, C., Suyker, A., Tagesson, T., Takanashi, S., Tang, Y., Tapper, N., Thom, J., Tiedemann, F., Tomassucci, M., Tuovinen, J.P., Urbanski, S., Valentini, R., van der Molen, M., van Gorsel, E., van Huissteden, K., Varlagin, A., Verfaillie, J., Vesala, T., Vincke, C., Vitale, D., Vygodskaya, N., Walker, J.P., Walter-Shea, E., Wang, H., Weber, R., Westermann, S., Wille, C., Wofsy, S., Wohlfahrt, G., Wolf, S., Woodgate, W., Li, Yuelin, Zampieri, R., Zhang, J., Zhou, G., Zona, D., Agarwal, D., Biraud, S., Torn, M., Papale, D., 2020. The FLUXNET2015 dataset and the ONEFlux processing pipeline for eddy covariance data. *Sci. Data* 7, 225. [10.1038/s41597-020-0534-3](https://doi.org/10.1038/s41597-020-0534-3).
- Paul-Limoges, E., Damm, A., Hueni, A., Liebsch, F., Eugster, W., Schaepman, M.E., Buchmann, N., 2018. Effect of environmental conditions on sun-induced fluorescence in a mixed forest and a cropland. *Remote Sens. Environ.* 219, 310–323. <https://doi.org/10.1016/J.RSE.2018.10.018>.
- Porcar-Castell, A., Malenovsky, Z., Magney, T., Van Wittenbergh, S., Fernández-Marín, B., Maignan, F., Zhang, Y., Maseyk, K., Atherton, J., Albert, L.P., Robson, T. M., Zhao, F., Garcia-Plazaola, J.I., Ensminger, I., Rajewicz, P.A., Grebe, S., Tikkanen, M., Kellner, J.R., Ihalainen, J.A., Rascher, U., Logan, B., 2021. Chlorophyll a fluorescence illuminates a path connecting plant molecular biology to Earth-system science. *Nat. Plants*. <https://doi.org/10.1038/s41477-021-00980-4>.

- Rannik, Ü., Sogachev, A., Foken, T., Göckede, M., Kljun, N., Leclerc, M.Y., Vesala, T., 2012. Footprint Analysis, in: Eddy Covariance. Springer, Dordrecht, pp. 211–261. https://doi.org/10.1007/978-94-007-2351-1_8.
- Raupach, M.R., 1994. Simplified expressions for vegetation roughness length and zero-plane displacement as functions of canopy height and area index. *Boundary-Layer Meteorol.* 71, 211–216. <https://doi.org/10.1007/BF00709229>.
- Ryu, Y., Berry, J.A., Baldocchi, D.D., 2019. What is global photosynthesis? History, uncertainties and opportunities. *Remote Sens. Environ.* 223, 95–114. <https://doi.org/10.1016/j.rse.2019.01.016>.
- Sadeh, Y., Zhu, X., Dunkerley, D., Walker, J.P., Zhang, Y., Rozenstein, O., Manivasagam, V.S., Chenu, K., 2021. Fusion of Sentinel-2 and PlanetScope time-series data into daily 3m surface reflectance and wheat LAI monitoring. *Int. J. Appl. Earth Obs.* 96, 102260. <https://doi.org/10.1016/j.jag.2020.102260>.
- Schickling, A., Matveeva, M., Damm, A., Schween, J.H., Wähler, A., Graf, A., Crewell, S., Rascher, U., 2016. Combining sun-induced chlorophyll fluorescence and photochemical reflectance index improves diurnal modeling of gross primary productivity. *Remote Sens.* 8. <https://doi.org/10.3390/rs8070574>.
- Sun, Y., Frankenberg, C., Wood, J.D., Schimel, D.S., Jung, M., Guanter, L., Drewry, D.T., Verma, M., Porcar-Castell, A., Griffis, T.J., Gu, L., Magney, T.S., Köhler, P., Evans, B., Yuen, K., 2017. OCO-2 advances photosynthesis observation from space via solar-induced chlorophyll fluorescence. *Science* (80-) 358, eaam5747. <https://doi.org/10.1126/science.aam5747>.
- Suyker, A.E., Verma, S.B., 2012. Gross primary production and ecosystem respiration of irrigated and rainfed maize-soybean cropping systems over 8 years. *Agric. For. Meteorol.* 165, 12–24. <https://doi.org/10.1016/j.agrformet.2012.05.021>.
- Thenkabaila, A., Lyon, P., Huete, J., Gitelson, A., 2011. Hyperspectral Vegetation Indices. In: *Hyperspectral Remote Sensing of Vegetation*, pp. 345–364. <https://doi.org/10.1201/b11222-21>.
- Turner, A.J., Köhler, P., Magney, T.S., Frankenberg, C., Fung, I., Cohen, R.C., 2020. A double peak in the seasonality of California's photosynthesis as observed from space. *Biogeosciences* 17, 405–422. <https://doi.org/10.5194/bg-17-405-2020>.
- Vickers, D., Mahrt, L., 1997. Quality control and flux sampling problems for tower and aircraft data. *J. Atmos. Ocean. Technol.* 14, 512–526. [https://doi.org/10.1175/1520-0426\(1997\)014<0512:QCAFSF>2.0.CO;2](https://doi.org/10.1175/1520-0426(1997)014<0512:QCAFSF>2.0.CO;2).
- Vieira, S.R., Gonzalez, A.P., 2003. Analysis of the spatial variability of crop yield and soil properties in small agricultural plots. *Bragantia* 62, 127–138. <https://doi.org/10.1590/S0006-87052003000100016>.
- Wang, X., Chen, J.M., Ju, W., 2020. Photochemical reflectance index (PRI) can be used to improve the relationship between gross primary productivity (GPP) and sun-induced chlorophyll fluorescence (SIF). *Remote Sens. Environ.* 246, 111888. <https://doi.org/10.1016/j.rse.2020.111888>.
- Webb, E.K., Pearman, G.I., Leuning, R., 1980. Correction of flux measurements for density effects due to heat and water vapour transfer. *Q. J. R. Meteorol. Soc.* 106, 85–100. <https://doi.org/10.1002/qj.49710644707>.
- Wen, J., Köhler, P., Duveiller, G., Parazoo, N.C., Magney, T.S., Hooker, G., Yu, L., Chang, C.Y., Sun, Y., 2020. A framework for harmonizing multiple satellite instruments to generate a long-term global high spatial-resolution solar-induced chlorophyll fluorescence (SIF). *Remote Sens. Environ.* 239. <https://doi.org/10.1016/j.rse.2020.111644>.
- Whitaker, J., Field, J.L., Bernacchi, C.J., Cerri, C.E.P., Ceulemans, R., Davies, C.A., DeLucia, E.H., Donnison, I.S., McCalmont, J.P., Paustian, K., Rowe, R.L., Smith, P., Thornley, P., McNamara, N.P., 2018. Consensus, uncertainties and challenges for perennial bioenergy crops and land use. *Glob. Change Biol. Bioenergy* 10, 150. <https://doi.org/10.1111/GCBB.12488>.
- Wu, G., Guan, K., Jiang, C., Kimm, H., Miao, G., Bernacchi, C.J., Moore, C.E., Ainsworth, E.A., Yang, X., Berry, J.A., Frankenberg, C., Chen, M., 2022a. Attributing differences of solar-induced chlorophyll fluorescence (SIF)-gross primary production (GPP) relationships between two C4 crops: corn and miscanthus. *Agric. For. Meteorol.* 323, 109046. <https://doi.org/10.1016/J.AGRFORMET.2022.109046>.
- Wu, G., Guan, K., Jiang, C., Peng, B., Kimm, H., Chen, M., Yang, X., Wang, S., Suyker, A. E., Bernacchi, C.J., Moore, C.E., Zeng, Y., Berry, J.A., Cendrero-Mateo, M.P., 2020. Radiance-based NIRv as a proxy for GPP of corn and soybean. *Environ. Res. Lett.* 15. <https://doi.org/10.1088/1748-9326/ab65cc>.
- Wu, G., Jiang, C., Kimm, H., Wang, S., Bernacchi, C., Moore, C.E., Suyker, A., Yang, X., Magney, T., Frankenberg, C., Ryu, Y., Dechant, B., Guan, K., 2022b. Difference in seasonal peak timing of soybean far-red SIF and GPP explained by canopy structure and chlorophyll content. *Remote Sens. Environ.* 279, 113104. <https://doi.org/10.1016/j.rse.2022.113104>.
- Yang, P., van der Tol, C., Campbell, P.K.E., Middleton, E.M., 2021. Unraveling the physical and physiological basis for the solar-induced chlorophyll fluorescence and photosynthesis relationship using continuous leaf and canopy measurements of a corn crop. *Biogeosciences* 18, 441–465.
- Yang, X., Shi, H., Stovall, A., Guan, K., Miao, G., Zhang, Yongguang, Zhang, Yao, Xiao, X., Ryu, Y., Lee, J.E., 2018. FluSpec 2—An automated field spectroscopy system to monitor canopy solar-induced fluorescence. *Sensors (Switzerland)* 18. <https://doi.org/10.3390/s18072063>.
- Yang, X., Tang, J., Mustard, J.F., Lee, J.E., Rossini, M., Joiner, J., Munger, J.W., Kornfeld, A., Richardson, A.D., 2015. Solar-induced chlorophyll fluorescence that correlates with canopy photosynthesis on diurnal and seasonal scales in a temperate deciduous forest. *Geophys. Res. Lett.* 42. <https://doi.org/10.1002/2015GL063201>.
- Yu, L., Wen, J., Chang, C.Y., Frankenberg, C., Sun, Y., 2018. High Resolution Global Contiguous Solar-Induced Chlorophyll Fluorescence (SIF) of Orbiting Carbon Observatory-2 (OCO-2) 2. [10.1029/2018GL081109](https://doi.org/10.1029/2018GL081109).
- Zeng, Y., Badgley, G., Dechant, B., Ryu, Y.Y., Chen, M., Berry, J.A.J.A.A., 2019. A practical approach for estimating the escape ratio of near-infrared solar-induced chlorophyll fluorescence. *Remote Sens. Environ.* 232, 111209. <https://doi.org/10.1016/j.rse.2019.05.028>.
- Zeng, Y., Chen, M., Hao, D., Damm, A., Badgley, G., Rascher, U., Johnson, J.E., Dechant, B., Siegmund, B., Ryu, Y., Qiu, H., Krieger, V., Panigada, C., Celesti, M., Miglietta, F., Yang, X., Berry, J.A., 2022a. Combining near-infrared radiance of vegetation and fluorescence spectroscopy to detect effects of abiotic changes and stresses. *Remote Sens. Environ.* 270, 112856. <https://doi.org/10.1016/j.rse.2021.112856>.
- Zeng, Y., Hao, D., Huete, A., Dechant, B., Berry, J., Chen, J.M., Joiner, J., Frankenberg, C., Bond-Lamberty, B., Ryu, Y., Xiao, J., Asrar, G.R., Chen, M., 2022b. Optical vegetation indices for monitoring terrestrial ecosystems globally. *Nat. Rev. Earth Environ.* 37 (3), 477–493. <https://doi.org/10.1038/s43017-022-00298-5>.
- Zhang, Q., Zhang, X., Li, Z., Wu, Y., Zhang, Y., 2019. Comparison of Bi-Hemispherical and Hemispherical-Conical Configurations for In Situ Measurements of Solar-Induced Chlorophyll Fluorescence. *Remote Sens.* 11, 2642. <https://doi.org/10.3390/rs11222642>, 2019, Vol. 11, Page 2642.
- Zhang, Y., Joiner, J., Hamed Alemohammad, S., Zhou, S., Gentile, P., 2018. A global spatially contiguous solar-induced fluorescence (CSIF) dataset using neural networks. *Biogeosciences* 15, 5779–5800. <https://doi.org/10.5194/bg-15-5779-2018>.
- Zhang, Y., Sun, K., Gao, Z., Pan, Z., Shook, M.A., Li, D., 2020. Diurnal Climatology of Planetary Boundary Layer Height Over the Contiguous United States Derived From AMDAR and Reanalysis Data. *J. Geophys. Res. Atmos.* 125. <https://doi.org/10.1029/2020JD032803>.
- Zhang, Y., Zhang, Q., Liu, L., Zhang, Y., Wang, S., Ju, W., Zhou, G., Zhou, L., Tang, J., Zhu, X., Wang, F., Huang, Y., Zhang, Z., Qiu, B., Zhang, X., Wang, Songhan, Huang, C., Tang, X., Zhang, J., 2021. ChinaSpec: A Network for Long-Term Ground-Based Measurements of Solar-Induced Fluorescence in China. *J. Geophys. Res. Biogeosciences* 126. <https://doi.org/10.1029/2020JG006042>.
- Zhang, Z., Zhang, Y., Porcar-Castell, A., Joiner, J., Guanter, L., Yang, X., Migliavacca, M., Ju, W., Sun, Z., Chen, S., Martini, D., Zhang, Q., Li, Z., Cleverly, J., Wang, H., Goulas, Y., 2020. Reduction of structural impacts and distinction of photosynthetic pathways in a global estimation of GPP from space-borne solar-induced chlorophyll fluorescence. *Remote Sens. Environ.* 240, 111722. <https://doi.org/10.1016/j.rse.2020.111722>.